Apical domain mechanosensation regulates tissue tension homeostasis

Naoya Hino[1,*], Tushna Kapoor[1], Uday Ram Gubbala[1], Édouard Hannezo[1], and Carl-Philipp Heisenberg[1,*]

[1]Institute of Science and Technology Austria, 3400 Klosterneuburg, Austria
[*]Correspondence: naoya.hino@ist.ac.at (N.H.), heisenberg@ist.ac.at (C.-P.H.)

Summary

Tissue tension is a key determinant of tissue shape, and its regulation is essential for both morphogenesis and the maintenance of tissue integrity. During zebrafish embryogenesis, the enveloping layer (EVL) – an epithelial monolayer covering the blastoderm – undergoes extensive spreading that is driven by pulling forces exerted at its margin and more than doubles its surface area. Yet whether and how the EVL actively regulates its tissue tension during this process remains unclear. Here, we show that the EVL maintains constant tissue tension while spreading, and that it achieves this by reducing apical cell contractility in response to the same pulling forces that drive its spreading. We identify a mechanosensitive pathway underlying this response, mediated by the scaffold/adaptor protein Kibra regulating the activity of atypical protein kinase C (aPKC) at the apical domain of EVL cells. Under low mechanical stretch, Kibra forms condensates at the base of actin-based apical projections, where it activates Myosin II to increase apical contractility through aPKC downregulation. As mechanical stretch increases, apical projections disassemble, Kibra condensates dissolve, and aPKC activity rises. Elevated aPKC activity in turn reduces apical contractility by reducing Myosin II activity, thereby maintaining constant tissue tension despite increased mechanical stretch. Together, these findings reveal a mechanosensitive mechanism that enables robust adaptation of tissue tension to changing mechanical stretch, ensuring efficient tissue spreading and morphogenesis.

Keywords

Epithelial spreading, tissue tension, mechanosensation, aPKC, Kibra, zebrafish

Introduction

Fine-tuning of tissue tension is important for the development of programmed morphologies during embryogenesis. Loss of tissue tension leads to unprogrammed deformation or fluctuation of tissue architecture[1–4], while excessive tissue tension tears the tissues and abrogates their integrity[5,6]. Furthermore, controlled tissue deformation relies on balancing tissue tension with the mechanical forces driving the deformation, and thus, adapting tissue tension to dynamic changes in the mechanical environment is critical for robust tissue morphogenesis.

In epithelial morphogenesis, tissue tension is built up by the interplay between cell adhesion and contractile forces[7,8]. Cell contractility is dependent on Myosin II activation, which is mainly regulated by phosphorylation of its regulatory light chain through kinases such as Rho-associated coiled-coil kinase (ROCK) or Myosin light-chain kinase (MLCK)[9]. These kinases are activated by various signaling pathways, depending on the tissue and cell types[10]. Atypical protein kinase C (aPKC), a signaling molecule that regulates the establishment and functionalization of the apical domain of epithelial cells, plays a key role in regulating epithelial tissue tension[5,11] through the regulation of Myosin II activity[12,13]. Yet, whether and how tension in epithelial tissues is modulated by mechanical forces driving tissue deformation remains elusive.

The enveloping layer (EVL), an epithelial monolayer covering the surface of the blastoderm in early zebrafish embryos, provides an excellent model system for investigating the mechanisms regulating force-dependent tissue deformation and tension modulation[14]. During epiboly, the EVL spreads over the large yolk cell (Fig. 1a,b). This process begins at the sphere stage (4 hours post fertilization, hpf) and continues until the EVL completely encloses the yolk cell at the bud stage (10 hpf)[15]. The driving force for epiboly is generated by a prominent actomyosin ring within the yolk syncytial layer (YSL), which pulls the EVL margin vegetally over the yolk cell surface[14]. Previous studies have shown that early epiboly movements depend on EVL cells reducing their tissue tension and undergoing oriented cell divisions, thereby relieving tension anisotropy during tissue spreading[6,16]. However, EVL cell divisions occur predominantly during early stages of epiboly[6,17] (Fig. 1c), raising the question of whether and by what mechanisms tissue tension is regulated during the later stages.

Results

EVL exhibits tissue tension homeostasis during epiboly

To determine how the EVL undergoes spreading during late epiboly stages in the absence of notable cell divisions, we analyzed EVL cell shape changes at the animal pole during the course of epiboly (6-10 hpf). We found that EVL cells increased their apical area by 2.2-fold from 6 to 9 hpf (Fig. 1d,e), indicative of considerable spreading of EVL cells during epiboly. To examine whether these EVL cell shape changes are triggered by actomyosin band contraction within the YSL, we reduced actomyosin contractility specifically within the YSL by injecting constitutively active myosin phosphatase (CA-Mypt) mRNA into the YSL. This not only delayed epiboly progression, as previously noted (Supplementary Fig.1a,b)[18], but also suppressed EVL cell spreading (Fig. 1f,g), indicating that EVL cell shape changes are triggered by pulling forces from the YSL.

To determine whether pulling force-induced EVL cell shape changes are accompanied by changes in EVL tissue tension, we asked how EVL tissue tension evolves over the course of epiboly. To this end, we measured EVL tension along the plane of the tissue at the animal pole by micropipette aspiration (Fig. 1h)[19]. We used large micropipettes with a diameter of 60 μm to ensure that multiple EVL cells were aspirated, and determined tissue-scale tension from the pressure required to hold a hemispherical cap of EVL tissue within the micropipette. Interestingly, we found that EVL tissue tension remained largely unchanged over the course of epiboly (Fig. 1i). Moreover, reducing pulling forces from the YSL by expressing CA-Mypt within the YSL had no major effect on EVL tissue tension, which remained constant over time (Fig. 1i), indicating tissue tension homeostasis irrespective of variations in the level of pulling forces acting on the EVL margin. This was surprising, as stretching an epithelial monolayer would be expected to increase its tissue tension. Indeed, minimal 3D vertex modelling[20–23] of EVL cell mechanics during epiboly (see Methods) predicted an increase in tissue tension proportional to cell apical area changes, such that tissue tension should increase over time in control embryos and be reduced in embryos expressing CA-Mypt within the YSL, where pulling forces are diminished (Fig. 1j,k). This discrepancy between theoretical prediction and experimental observation suggests the existence of an active feedback mechanism that enables tissue tension homeostasis in the EVL.

Pulling force-dependent reduction in contractility through aPKC activation regulates tissue tension homeostasis

Theoretically, tissue tension is a product of global tissue deformation and local cell contractility (see Methods). To understand how the EVL achieves tissue tension homeostasis during epiboly, we therefore turned to Myosin II, a key regulator of cell contractility and tissue tension[9,10]. To test whether Myosin II is involved in EVL tension homeostasis, we monitored its subcellular localization in EVL cells of Tg(*actb2:Myl12.1-EGFP*) embryos during epiboly. This revealed that Myosin II is localized not only at cell-cell junctions but also at the apical domain as puncta, which progressively dissolved over the course of epiboly (Fig. 2a,b). To determine whether this loss of apical Myosin II is driven by pulling forces from the YSL, we reduced these forces by injecting CA-Mypt mRNA into the YSL. In CA-Mypt-injected embryos, the progressive decrease in apical Myosin II localization was markedly suppressed (Fig. 2c,d), indicating that YSL-derived pulling forces mediate apical Myosin II disassembly in EVL cells, and that this reduction in apical Myosin II may underlie the fine-tuning of cell contractility required for tissue tension homeostasis during epiboly.

To address this hypothesis, we searched for upstream regulators of apical Myosin II that could mediate the effect of pulling forces on its apical localization in EVL cells. Given the well-documented roles of aPKC in regulating epithelial polarity and mechanics[11,12], we first examined whether aPKC might be involved in this process. To this end, we interfered with aPKC activity in EVL cells by injecting mRNA encoding a dominant-negative form of aPKC (DN-aPKC) together with fluorescently labeled dextran into a single blastomere at the animal pole of 64-cell stage embryos, and selected embryos displaying clones of fluorescently labeled EVL cells (Fig. 2e). DN-aPKC-expressing EVL cell clones showed more pronounced apical Myosin II localization compared to dextran-only controls (Fig. 2f,g). This increase in apical Myosin II was abolished upon the co-injection of CA-Mypt mRNA to reduce Myosin II activity (Fig. 2f,g). Conversely, expression of a constitutively active form of aPKC (CA-aPKC) in EVL cell clones caused a premature reduction in apical Myosin II (Fig. 2h,i). Taken together, these findings suggest that aPKC might mediate the effect of YSL-derived pulling forces on apical Myosin II localization and contractility.

To further test whether aPKC activity is modulated by YSL pulling forces, we monitored the subcellular localization of Par3 in EVL cells by injecting pard3ab-EGFP mRNA at the 1-cell stage, since the apical depletion of Par3 has previously been shown to be a readout of aPKC activation (Supplementary Fig. 2a)[24,25]. Consistent with pulling force-mediated aPKC activation, apical Par3 localization decreased over the course of epiboly (Supplementary Fig.

2a,b), and this reduction was suppressed upon YSL injection of CA-Mypt mRNA (Supplementary Fig. 2c,d). Furthermore, the co-injection of CA-aPKC mRNA caused a premature decrease in apical Par3 localization (Supplementary Fig. 2e,f). Together, these results suggest that aPKC activation downstream of YSL pulling forces controls apical Myosin II localization and contractility in EVL cells.

To examine whether force-dependent activation of aPKC regulates EVL tissue tension, we injected DN-aPKC mRNA at the 1-cell stage and assessed changes in EVL tissue tension by micropipette aspiration (Fig. 2j). Whereas control embryos maintained homeostatic EVL tissue tension, DN-aPKC-expressing embryos showed a steady increase in tissue tension over the course of epiboly. Notably, this tension increase was suppressed by reducing YSL pulling forces through CA-Mypt mRNA injection into the YSL. These results suggest that force-dependent modulation of aPKC activity is required for EVL tissue tension homeostasis.

To assess the consequences of disrupted tissue tension homeostasis upon aPKC downregulation, we analyzed epiboly progression in DN-aPKC-expressing embryos (Fig. 2k,l). These embryos exhibited delayed epiboly and, in some cases, local ruptures of the EVL upon completion of epiboly (Fig. 2k,l and Supplementary Video 1). Consistent with this, DN-aPKC–expressing EVL cells, injected at the 64-cell stage, had smaller apical area than controls, a phenotype rescued by co-expression of CA-Mypt (Fig. 2m,n). Together, these findings demonstrate that aPKC-mediated regulation of cell contractility enables tissue tension homeostasis, thereby promoting efficient EVL cell and tissue spreading while preserving tissue integrity.

To test whether mechanosensitive activation of aPKC is sufficient to account for the observed EVL tissue tension homeostasis, we incorporated this feedback mechanism (Fig. 2o) into a physical framework based on a minimal vertex model of 3D EVL cell mechanics (see Methods)[20,21,26,27]. In this model, force-dependent aPKC activation establishes a mechanosensitive coupling whereby cell deformation reduces apical contractility. As cells spread and thin during epiboly, increasing cell deformation would, in the absence of feedback, progressively increase tissue tension. However, because cell deformation simultaneously activates aPKC, which lowers apical contractility, this tension increase is counteracted. At intermediate coupling strengths, these opposing effects balanced one another, resulting in near-constant tissue tension throughout epiboly (Fig. 2p–r). The model further predicted that tissue tension homeostasis would be maintained upon reducing the YSL pulling force, consistent with our experimental observations in embryos expressing CA-Mypt in the YSL (Fig. 1i and Fig.

2p). Conversely, weakening the coupling between cell deformation and apical contractility, corresponding to DN-aPKC expression, resulted in elevated tissue tension and reduced apical spreading, closely recapitulating the phenotype of DN-aPKC-expressing embryos (Fig. 2j–n,p–r).

Taken together, our model supports the notion that pulling force-mediated aPKC activation counteracts tension buildup within the EVL by downregulating Myosin II activity, thereby maintaining tissue tension homeostasis and promoting epiboly progression (Fig. 2o–r).

Pulling force-dependent Kibra condensate dissolution is responsible for aPKC-mediated reduction in cell contractility and tissue tension homeostasis

To investigate how mechanical pulling forces regulate aPKC activity in EVL cells, we focused on Kibra, a known negative regulator of aPKC kinase activity in epithelial cells[28]. Kibra has previously been shown to form biomolecular condensates at the apical domain of epithelial cells, where it regulates Hippo signaling[29,30]. We therefore hypothesized that Kibra condensates might also modulate aPKC activity in EVL cells. To test this hypothesis, we first examined Kibra localization by expressing mNeonGreen–Kibra in EVL cells (Fig. 3a). Kibra formed discrete condensates at the apical domain. These condensates were slightly enriched in aPKC, which otherwise displayed a broad apical distribution in EVL cells (Fig. 3b). Notably, Kibra condensates progressively disassembled during epiboly (Fig. 3c,d), raising the possibility that pulling forces exerted by the YSL promote condensate disassembly. To directly assess this, we reduced YSL-generated pulling forces by injecting CA-Mypt mRNA into the YSL and analyzed Kibra localization (Fig. 3e). In CA-Mypt–injected embryos, the disassembly of Kibra condensates during epiboly was significantly suppressed (Fig. 3e,f), indicating that YSL-derived pulling forces drive Kibra condensate disassembly in EVL cells.

To determine whether pulling force-dependent Kibra condensate disassembly is functionally linked to the observed downregulation of EVL apical contractility, and consequently to EVL cell spreading during epiboly, we generated Kibra mutant constructs lacking either the coiled-coil domain (ΔCC), which is required for condensate formation[29], or the aPKC-binding region (ΔaBR)[28,31]. Consistent with previous reports, Kibra ΔCC failed to form condensates in EVL cells (Fig. 3g,h). In contrast, Kibra ΔaBR retained the ability to form condensates, although these were less prominent than those formed by control Kibra (Fig. 3g,h), indicating that aPKC binding is not strictly required for condensate formation itself.

To test whether Kibra regulates EVL cell contractility and to assess the functional importance of condensate formation and aPKC binding in this process, we overexpressed control Kibra, Kibra ΔCC, or Kibra ΔaBR in EVL cells by injecting the corresponding mRNAs into a single blastomere at the 64-cell stage, thereby generating mosaic EVL clones, and subsequently analyzed apical Myosin II localization (Fig. 3i). To achieve robust and reproducible expression in EVL cells, all constructs carried a mutation in the Kibra degron motif (S643A), previously shown to stabilize Kibra protein levels[32] (Supplementary Fig. 4a,b). mRNA concentrations were further adjusted to obtain comparable expression levels among the different constructs (Supplementary Fig. 4c).

Overexpression of control Kibra increased apical Myosin II accumulation and reduced EVL cell apical area (Fig. 3i–k), consistent with the proposed role of Kibra in suppressing aPKC activity. In contrast, overexpression of either Kibra ΔCC or Kibra ΔaBR failed to efficiently promote apical Myosin II accumulation or reduce EVL cell apical area (Fig. 3i–k). Together, these findings indicate that both condensate formation and aPKC binding are required for Kibra-mediated regulation of apical Myosin II contractility and, consequently, EVL cell spreading during epiboly.

To examine whether Kibra regulates EVL tissue tension, we overexpressed full length (FL) Kibra, Kibra ΔCC, or Kibra ΔaBR carrying the mutation at the degron motif (S643A) by injecting corresponding mRNAs at the 1 cell stage. Whereas control embryos exhibited homeostatic EVL tissue tension, FL Kibra-expressing embryos showed a time-dependent increase in tissue tension during epiboly (Fig. 3l), consistent with the effect of DN-aPKC expression (Fig. 2j) and thus Kibra's inhibitory effect on aPKC activity. Interestingly, this tension increase was not observed in the embryos injected with Kibra ΔCC or Kibra ΔaBR mRNAs. This supports the notion that Kibra condensates increase EVL tissue tension through the regulation of aPKC.

Pulling force triggers disassembly of Kibra-associated apical projections

We next asked how pulling forces regulate the disassembly of Kibra condensates in EVL cells. Following up on previous findings that Kibra distribution is associated with actomyosin flows[33], we hypothesized that Kibra condensate disassembly is triggered by alterations in the actin cytoskeletal architecture in EVL cells. To test this hypothesis, we investigated the dynamics of the actin cytoskeleton in EVL cells of Tg*(actb2:Lifeact-EGFP)* embryos during the course of epiboly (Fig. 4a). This showed that actin filaments were predominantly localized at the apical surface and cell-cell junctions in EVL cells. Cross-sectional images revealed that the actin

filaments at the apical surface of EVL cells protruded perpendicularly from the plasma membrane, resembling actin-based apical projections in epithelial cells[34]. This notion was further supported by electron microscopy images of EVL cells showing protruding structures at their apical domain (Fig. 4c). Interestingly, these structures were disassembled during the course of epiboly (Fig. 4a–c), indicating a progressive decrease of apical projections during EVL spreading. To address whether this disassembly of apical projections is triggered by the YSL pulling on the EVL, we reduced YSL pulling forces by injecting CA-Mypt mRNA into the YSL. In CA-Mypt–injected embryos, apical projections disassembly in EVL cells during epiboly was significantly suppressed (Fig. 4d,e), indicating that forces pulling on the EVL margin trigger apical projection disassembly in EVL cells.

To determine whether and how the loss of apical projections might be related to the loss of apical Kibra localization during epiboly, we performed high-resolution imaging of EVL cells in which both Kibra and actin filaments were labeled (Fig. 4f). Interestingly, the localization of Kibra condensates and apical projections was mutually exclusive, with Kibra condensates preferentially localizing directly adjacent to the base of apical projections (Fig. 4f), indicating a close spatial proximity, but not overlap, between Kibra condensates and apical projections.

Apical projection disassembly triggers Kibra condensate dissolution

To determine whether actin-based apical projections are required for apical Kibra condensate formation, we examined how perturbation of apical projection assembly affects Kibra condensation. To interfere with apical projection formation in EVL cells, we reduced Myosin II activity by expressing constitutively active Mypt (CA-Mypt), which in zebrafish periderm cells, the descendants of EVL cells, has previously been shown to suppress apical microridge formation[12,35]. In EVL cell clones co-expressing mNeonGreen-Kibra and CA-Mypt, both actin-based apical projections and adjacent Kibra condensates were strongly reduced (Fig. 5a–c). Importantly, despite the overall reduction in apical projections and Kibra condensates in CA-Mypt–expressing cells, the intensities of the remaining apical projections and associated Kibra condensates remained strongly positively correlated, similar to the relationship observed in control cells (Fig. 5d). These findings indicate that Kibra condensate formation is tightly coupled to the presence of actin-based apical projections.

Importantly, Kibra condensates were detected exclusively adjacent to apical projections, irrespective of the total number of apical projections present in either control or CA-Mypt–expressing EVL cells (Fig. 5a). This observation suggested that apical Kibra condensate formation depends on the presence of nearby apical projections. Consistent with this idea,

spatial cross-correlation analysis between Kibra condensates and apical projections revealed that the average distance separating these structures remained unchanged between control and CA-Mypt–expressing EVL cells (Fig. 5e,f), indicating that the spatial coupling between Kibra condensates and apical projections is maintained even when apical projection abundance is reduced.

These findings raised the possibility that actin-based apical projections actively promote the apical localization and/or formation of Kibra condensates. To test this hypothesis independently of Myosin II inhibition, we disrupted apical projection formation using alternative approaches and examined the resulting effects on apical Kibra localization. Based on a previous report showing that inhibition of exocytosis reduces apical projection formation[36], we treated embryos with the exocytosis inhibitor Endosidin-2, as well as with the actin polymerization inhibitor Cytochalasin D. Notably, both treatments led to a strong reduction in apical projection abundance accompanied by a corresponding decrease in Kibra condensate formation in EVL cells (Fig. 5g–l). Together, these findings indicate that the formation and maintenance of apical Kibra condensates depend on adjacent apical projection and suggest that pulling force-dependent loss of apical projection drives Kibra condensate disassembly during epiboly.

Discussion

By demonstrating that the pulling forces driving tissue spreading attenuate apical myosin contractility, thereby counteracting the stretch-induced increase in tension to achieve tissue tension homeostasis, we have identified an apical domain-mediated mechanosensitive mechanism essential for efficient tissue spreading and the maintenance of tissue integrity (Fig. 5m). Given the widespread and evolutionarily conserved role of the apical domain across epithelial tissues, this mechanism offers a unifying principle for epithelial morphogenesis, whereby tissue tension is precisely regulated to achieve stereotyped tissue architecture.

Our findings reveal that the apical domain functions not only as a regulator of tissue mechanics, as demonstrated in previous studies[11,12], but also as a sensor of epithelial stretch, enabling precise tuning of tissue tension. A minimal vertex model incorporating this mechanosensitive coupling between cell stretch and apical contractility recapitulates homeostatic behavior and its failure upon perturbation. This active mechanical buffering under stretch is reminiscent of actomyosin-driven stress relaxation in stretched epithelial monolayers[37] and the tensional plateau sustained over large areal strains in pressurized epithelia[23], suggesting it may represent a general physical principle of epithelial tissues undergoing force-driven morphogenesis. The

model further reveals that homeostasis requires the mechanosensitive feedback to operate within a specific parameter regime: insufficient feedback strength, as in embryos overexpressing DN-aPKC, results in monotonically rising tension, while excessive feedback drives a runaway loop in which stretch-induced myosin loss further reduces resistance and permits uncontrolled cell deformation. Whether this optimal regime reflects a general constraint on mechanosensitive epithelia is an interesting open question.

We show that pulling force-dependent disassembly of Kibra condensates at the apical domain reduces apical contractility through the regulation of aPKC, a key effector of apical domain remodeling. This is consistent with previous studies of *Drosophila* follicular epithelium morphogenesis, which proposed that Kibra condensate formation is dependent on epithelial cell strain[30,38]. Our study now provides a mechanistic basis for how pulling forces govern apical Kibra localization, demonstrating that Kibra condensate disassembly is triggered not by simple dilution of apical domain components consequent to apical expansion, but rather by stretch-dependent disassembly of actin-based apical projections, at the base of which Kibra condensates reside.

Notably, the base of apical projections, such as microvilli, is anchored in a cytoskeletal meshwork known as the terminal web, composed of structural proteins including myosins and spectrins[39]. Spectrins have previously been shown as important regulators of the Hippo signaling pathway[40,41], which itself depends on Kibra condensate formation[29,30], and as mechanoresponsive components of the membrane cytoskeleton[42,43]. Future studies will be needed to explore whether Kibra condensates associate with components of the terminal web, and how pulling forces modulate this association through stretch-dependent disassembly of apical projections.

Previous studies have established Kibra condensates as important regulators of Hippo signaling[29,30] and demonstrated that Kibra controls tissue growth and size by regulating cell proliferation and apoptosis through the Hippo pathway[44,45]. Our findings uncover an additional role for Kibra condensates in modulating cell and tissue mechanics in response to pulling forces. Together, these observations raise the intriguing possibility that Kibra coordinates tissue growth and morphogenesis not only through the regulation of cell number, but also by controlling tissue mechanical properties.

The pulling force-dependent reduction in cell contractility identified in our study carries an inherent risk: the system overshoots and the tissue deforms uncontrolledly under mechanical loading, rendering tissue morphology vulnerable to unprogrammed external forces. We

therefore propose that an additional feedback mechanism must exist to prevent excessive deformation. In support of this notion, acute mechanical stretching has been shown to activate myosin, increasing cell contractility and tissue tension[46–48], thereby helping to maintain tissue shape under mechanical load. Notably, the magnitude and rate of applied mechanical strain have recently been shown to determine the cellular response to mechanical loading, resulting in either increased or decreased contractility[49]. This raises the possibility that epithelial cells reduce apical contractility in response to moderate pulling forces, while upregulating contractility when forces or deformation exceed a certain threshold. An important question for future studies will therefore be how epithelial tissues distinguish the magnitude and rate of mechanical loading to tune their response accordingly, ensuring efficient and robust tissue morphogenesis during embryonic development. Notably, a recent study proposed that mechanical stretching of *Drosophila* follicle cells triggers apical constriction through aPKC downregulation[50], raising the intriguing possibility that aPKC may mediate both stretch-dependent increases and decreases in contractility depending on cellular context – a question that warrants further investigation.

Main figure titles and legends

Figure 1. EVL exhibits tissue tension homeostasis during epiboly.

a, A schematic of a zebrafish embryo at 50% (5 hpf, left) and 75% (7.5 hpf, right) epiboly stages. Black arrows mark the direction of EVL epiboly movements. In the left panel, a high magnification cross-section of the region outlined by the orange dashed rectangle is shown. The contraction of the actomyosin ring, positioned within the YSL at the EVL-YSL interface, drives EVL spreading by pulling the EVL margin toward the vegetal pole. EVL, Enveloping layer; YSL, Yolk syncytial layer. **b**, Maximum intensity projection images of a Tg*(actb2: Utrophin-mCherry)* embryo, labeling F-actin, at 6, 7.5, and 9 hours post-fertilization (hpf). Yellow arrowheads indicate the actomyosin ring formed within the YSL. Scale bar, 200 μm. **c**, Line plot of EVL cell proliferation rate normalized by cell number as a function of time during epiboly. Mean ± standard deviation (SD). n = 6 embryos from 3 independent experiments. **d**, Fluorescence images of EVL cells in a Tg*(actb2:mCherry-CAAX)* embryo labeling the plasma membrane at 6, 7.5, and 9 hpf. Top (x-y section) and lateral (x-z section) views are shown for each time point. Representative EVL cells in the lateral views are outlined by blue dashed lines. Scale bar, 20 μm. **e**, Dot plot of EVL cell apical area at 6, 7.5, and 9 hpf. n = 173 cells (6 hpf), n = 91 cells (7.5 hpf), n = 67 cells (9 hpf) from 3 independent experiments. One-way ANOVA followed by Dunnett's multiple comparisons test; ****$p < 0.0001$ for 6 hpf vs. 7.5 hpf and 6 hpf vs. 9 hpf. **f**, Fluorescence images of EVL cells at 8 hpf in a Tg*(actb2:mCherry-CAAX)* embryo, labeling the plasma membrane, injected with 25 pg H2A-mCherry mRNA (control) or 25 pg H2A-mCherry and 150 pg CA-Mypt mRNA (to reduce actomyosin contraction within the YSL) into the YSL at 3.3 hpf. Top (x-y section) and lateral (x-z section) views are shown for each condition. Representative EVL cells in the lateral views are outlined by blue dashed lines. Scale bar, 20 μm. **g**, Dot plot of EVL cell apical area for the conditions described in **f**. n = 82 cells (control), n = 183 cells (CA-Mypt) from 3 independent experiments. Welch's t-test; ****$p < 0.0001$. **h**, A schematic of micropipette aspiration assay (MPA) for the measurement of EVL tissue tension. EVL at the animal pole is aspirated by applying negative pressure. The bright-field image on the right shows aspirated EVL. Scale bar, 30 μm. **i**, Dot plot of EVL tissue tension at 6 and 9 hpf, obtained by the MPA on embryos injected with 25 pg H2A-mCherry mRNA (control) or 25 pg H2A-mCherry and 150 pg CA-Mypt mRNA into the YSL (to reduce actomyosin contraction within the YSL) at 3.3 hpf. n = 18 embryos for each condition from 3 independent experiments. One-way ANOVA followed by Tukey's multiple comparisons test; $p = 0.9678$ for 6 hpf (control) vs. 9 hpf (control); ***$p = 0.0003$ for 6 hpf (control) vs. 6 hpf (CA-Mypt); $p = 0.2674$ for 9 hpf (control) vs. 9 hpf (CA-Mypt). **j**, Schematic of the minimal vertex model of EVL cell mechanics. Left: the EVL is represented as a layer of

prismatic cells, each described by an apical radius r and height h. Right: tissue tension γ is set by the balance between active apical tension (T_a), basal tension (T_b), and lateral cortical tension (Γ_l), with the actomyosin ring exerting an increasing pulling force σ_{ring} at the EVL margin. From the Young-Laplace relation applied to the prism geometry, $\gamma = 2T_a - \Gamma_l \cdot h/r$. **k**, Tissue tension (normalized to the values at t = 6 hpf) predicted by this geometric model assuming constant apical contractility T_a (i.e., no mechanosensitive regulation). As the ring force drives cell spreading, h/r decreases and γ is therefore expected to rise passively. Dashed lines show the predicted tension in the absence of T_a regulation: for control embryos (red), in which the ring force exceeds tissue tension at t = 6 hpf ($\sigma_{ring}(t = 0) > \gamma_{t=0}$), rapid spreading is predicted, resulting in a large tension increase. For CA-Mypt YSL embryos (green), in which reduced YSL contractility ($\sigma_{ring}(t = 0) = \gamma_{t=0}$) slows spreading, a smaller but still substantial rise in tension is predicted. Solid blue: experimentally measured tissue tension, which remains approximately constant throughout epiboly. The discrepancy between the predicted and experimentally measured tissue tension profiles motivates an active mechanosensitive circuit that counteracts the passive tension increase.

Figure 2. Pulling force-dependent reduction in contractility through aPKC activation regulates tissue tension homeostasis.

a, Fluorescence images of EVL cells in a Tg*(actb2:Myl12.1-EGFP)* embryo, labeling Myosin II at 6, 7, 8, and 9 hpf. Top (apical surface projection of x-y section; upper panel) and lateral (x-z section; lower panel) views are shown for each time point. Magnified images of the regions demarcated by white squares are shown in the lower-left corner of each image. Scale bar, 20 μm. **b**, Dot plot of mean apical Myosin II intensity at 6, 7, 8, and 9 hpf. n = 107 cells (6 hpf), n = 60 cells (7 hpf), n = 42 cells (8 hpf), n = 39 cells (9 hpf) from 3 independent experiments. One-way ANOVA followed by Dunnett's multiple comparisons test; ****p < 0.0001 for 6 hpf vs. 7, 8, or 9 hpf. **c**, Fluorescence images of EVL cells at 8 hpf in a Tg*(actb2:Myl12.1-EGFP)* embryo injected with 25 pg H2A-mCherry mRNA (control) or 25 pg H2A-mCherry together with 150 pg CA-Mypt mRNA (to reduce actomyosin contraction within the YSL) into the YSL at 3.3 hpf. Top (apical surface projection of x-y section; upper panel) and lateral (x-z section; lower panel) views are shown for each condition. Scale bar, 20 μm. **d**, Dot plot of mean apical Myosin II intensity for the conditions described in **c**. n = 60 cells (control), n = 145 cells (CA-Mypt) from 3 independent experiments. Welch's t-test; ****p < 0.0001. **e**, A schematic of 64-cell stage injection: at the 64-cell stage (2 hpf), a single blastomere at the animal pole is injected with mRNA and fluorescent dextran (green). Fluorescently labeled EVL clones are imaged at

later stages of epiboly (bottom). **f**, Fluorescence images of EVL cell clones injected at the 64-cell stage with 16.4 pg dextran Alexa Fluor 594 (control), 16.4 pg dextran Alexa Fluor 594 and 19.6 pg DN-aPKC mRNA (DN-aPKC; to reduce aPKC activity), or a combination of 16.4 pg dextran Alexa Fluor 594, 19.6 pg DN-aPKC mRNA, and 9.8 pg CA-Mypt mRNA (DN-aPKC + CA-Mypt, to reduce both aPKC and Myosin II activities) in a Tg*(actb2:Myl12.1-EGFP)* embryo at 9 hpf. Apical surface projection images of Myl12.1-EGFP (top) and dextran Alexa Fluor 594 (bottom) are shown for each condition. Scale bar, 20 μm. **g**, Dot plot of mean apical Myosin II intensity for the conditions described in **f**. n = 40 cells (control), n = 34 cells (DN-aPKC), and n = 19 (DN-aPKC + CA-Mypt) from 3 independent experiments. One-way ANOVA followed by Dunnett's multiple comparisons test; ****$p < 0.0001$ for control vs. DN-aPKC; $p = 0.4282$ for control vs. DN-aPKC + CA-Mypt (not significant, n.s.). **h**, Fluorescence images of EVL cell clones injected at the 64-cell stage with 16.4 pg dextran Alexa Fluor 594 (control) or 16.4 pg dextran Alexa Fluor 594 and 6.5 pg CA-aPKC mRNA (CA-aPKC, to increase aPKC activity) in a Tg*(actb2:Myl12.1-EGFP)* embryo at 6 hpf. Apical surface projection images of Myl12.1-EGFP (top) and dextran Alexa Fluor 594 (bottom) are shown for each condition. **i**, Dot plot of mean apical Myosin II intensity for the conditions described in **h**. n = 83 cells (control), n = 81 cells (CA-aPKC) from 3 independent experiments. Welch's t-test; ****$p < 0.0001$. **j**, Dot plot of EVL tissue tension measured at the indicated time points, obtained by micropipette aspiration assay in embryos injected with 0.05% Phenol Red (control) or 0.05% Phenol Red and 300 pg DN-aPKC mRNA (DN-aPKC, to decrease aPKC activity) at the 1-cell stage. Embryos injected with 300 pg DN-aPKC mRNA at the 1-cell stage were further injected into the YSL at 3.3hpf with 25 pg H2A-mCherry mRNA (control YSL), or 25 pg H2A-mCherry and 150 pg CA-Mypt mRNA (CA-Mypt YSL). n = 21 embryos for 6 hpf (control), n = 20 embryos for 9 hpf (control), 6 hpf (DN-aPKC), and 9 hpf (DN-aPKC), and n = 18 embryos for DN-aPKC with control and CA-Mypt YSL injections from 3 independent experiments. One-way ANOVA followed by Tukey's multiple comparisons test; $p = 0.8888$ (n.s.) for 6 hpf (control) vs. 9 hpf (control); ****$p < 0.0001$ for 6 hpf (DN-aPKC) vs. 9 hpf (DN-aPKC) and for 9 hpf (DN-aPKC; control YSL) vs. 9 hpf (DN-aPKC; CA-Mypt YSL). **k**, Maximum intensity projection images of Tg*(actb2: Utrophin-mCherry)* embryos, labeling F-actin, injected with 0.05% Phenol Red (control, top) or 300 pg DN-aPKC mRNA (DN-aPKC, bottom) at 7 and 9 hpf. Scale bar, 200 μm. **l**, Line plot of EVL epiboly progression as a function of time during epiboly for the conditions described in **k**. Blue and orange lines indicate control and DN-aPKC embryos, respectively. Mean ± SD. n = 9 embryos for each condition from 3 independent experiments. **m**, Fluorescence images of EVL cell clones injected at the 64-cell stage with 16.4 pg dextran fluorescein (control), 16.4 pg dextran fluorescein and 19.6 pg DN-

aPKC mRNA (DN-aPKC, to reduce aPKC activity), or 16.4 pg dextran fluorescein together with 19.6 pg DN-aPKC mRNA and 9.8 pg CA-Mypt mRNA (DN-aPKC + CA-Mypt, to reduce both aPKC and Myosin II activities) in a Tg*(actb2:mCherry-CAAX)* embryo at 9 hpf. Top (x-y section; upper panel) and lateral (x-z section; lower panel) views are shown for each condition. Representative EVL cells in the lateral views are outlined by blue dashed lines. Scale bar, 20 μm. **n**, Dot plot of EVL cell apical area for the conditions described in **m**. n = 60 cells (control), n = 82 cells (DN-aPKC), n = 49 cells (DN-aPKC + CA-Mypt) from 3 independent experiments. One-way ANOVA followed by Dunnett's multiple comparisons test; ****p < 0.0001 for control vs. DN-aPKC; **p = 0.0047 for control vs. DN-aPKC + CA-Mypt. **o**, Mechano-chemical circuit of the minimal vertex model (see Supplementary Fig. 3a). Cell stretch (ε) activates aPKC, suppressing Myosin II (M) with sensitivity β and timescale τ_M; Myosin II in turn drives apical contractility (T_a) via a Hill function (coupling constant Σ, exponent n); tissue tension resists further stretch through drag η, closing the negative-feedback loop. YSL ring force σ_{ring} (ramp rate k_f) serves as the external mechanical input. **p**, Line plots of EVL tissue tension (normalized to control at t = 6 hpf) from vertex model simulations for control (full mechanosensing, $\sigma_0 = \gamma_0 + \Delta$; blue, solid), CA-Mypt YSL (reduced ring force during spreading, $\sigma_0 = \gamma_0$, mechanosensing intact; green, dashed), DN-aPKC (no stretch-mediated Myosin II downregulation, M frozen; orange, dash-dot), and DN-aPKC + CA-Mypt YSL (both perturbations combined, M frozen, $\sigma_0 = \gamma_0$; yellow, dotted) conditions, from 6 to 9 hpf. **q**, Line plots of EVL cell apical area (normalized to control at t = 6 hpf) from vertex model simulations for control, CA-Mypt YSL, and DN-aPKC conditions as in (**p**). **r**, Line plots of apical Myosin II levels (M; assumed to represent apical contractility T_a) from vertex model simulations for control, CA-Mypt YSL, and DN-aPKC conditions as in (**p**). See Methods and parameter table for full details.

Figure 3. Pulling force-dependent Kibra condensate dissolution is responsible for the aPKC-mediated reduction in cell contractility and tissue tension homeostasis

a, Fluorescence images of EVL cells in an embryo injected with 200 pg mNeonGreen-wwc1 mRNA at the 1-cell stage to visualize Kibra at 6 hpf. Upper left panel: Apical surface projection of x-y sections (top view). Upper right panel: the x-y section containing nuclei (top view). Lower left panel: lateral view (x-z section); a magnified image of the region demarcated by a white square is shown in the lower-left corner. Scale bar, 20 μm. **b**, Fluorescence images of EVL cells in a Tg*(actb2: mCherry-HA-prkci)* embryo, labeling aPKC, injected with 200 pg mNeonGreen-wwc1 mRNA to visualize Kibra at 6 hpf. Left panel: Kibra. Middle panel: aPKC.

Right panel: Merge of Kibra (green) and aPKC (magenta). Scale bar, 20 μm. **c**, Fluorescence images of EVL cells in an embryo injected with 200 pg mNeonGreen-wwc1 mRNA at the 1-cell stage to visualize Kibra at 6, 7, 8, and 9 hpf. Apical surface projection of x-y sections is shown for each time point. Scale bar, 20 μm. **d**, Dot plot of mean apical Kibra intensity at 6, 7, 8, and 9 hpf. n = 182 cells (6 hpf), n = 119 cells (7 hpf), n = 74 cells (8 hpf), n = 49 cells (9 hpf) from 3 independent experiments. One-way ANOVA followed by Dunnett's multiple comparisons test; ****$p < 0.0001$ for 6 hpf vs. 7, 8, or 9 hpf. **e**, Fluorescence images of EVL cells at 8 hpf in an embryo injected with 200 pg mNeonGreen-wwc1 mRNA at the 1-cell stage to visualize Kibra, and injected with 25 pg H2A-mCherry mRNA (control YSL, left panel) or 25 pg H2A-mCherry and 150 pg CA-Mypt mRNA (CA-Mypt YSL; to reduce actomyosin contraction within the YSL, right panel) into the YSL at the 3.3 hpf. Apical surface projection of x-y sections is shown for each condition. Scale bar, 20 μm. **f**, Dot plot of mean apical Kibra intensity for the conditions described in **e**. n = 97 cells (control YSL), n = 176 cells (CA-Mypt YSL) from 3 independent experiments. Welch's t-test; ****$p < 0.0001$. **g**, Fluorescence images of EVL cells in embryos injected at the 64-cell stage with 200 pg (142 amol) mNeonGreen-wwc1, 152 pg (142 amol) mNeonGreen-wwc1 ΔCC mRNA, or 193 pg (142 amol) mNeonGreen-wwc1 ΔaBR mRNA at the 1-cell stage to visualize wild type (WT) Kibra and Kibra deletion mutants at 6 hpf. Apical surface projection of x-y sections is shown for each condition. **h**, Dot plot of mean apical Kibra (WT and deletion mutants) intensities for the conditions described in **g**. n = 59 cells (WT), n = 61 cells (ΔCC), and n = 71 cells (ΔaBR) from at least 3 independent experiments. One-way ANOVA followed by Dunnett's multiple comparisons test; ****$p < 0.0001$ for WT vs. ΔCC or ΔaBR. **i**, Fluorescence images of EVL cell clones injected at the 64-cell stage with 16.4 pg dextran fluorescein (control), 19.6 pg (13.9 amol) mNeonGreen-wwc1 S643A mRNA (FL; full length), 9.9 pg (9.2 amol) mNeonGreen-wwc1 S643A ΔCC mRNA (ΔCC), or 12.7 pg (9.2 amol) mNeonGreen-wwc1 S643A ΔaBR mRNA (ΔaBR) in a Tg*(actb2:myl12.1-mCherry)* embryo, at 8 hpf. Apical surface projection images of Myl12.1-mCherry (top) and dextran fluorescein or mNeonGreen-Kibra S643A (bottom) are shown for each condition. Scale bar, 20 μm. **j**, Dot plot of mean apical Myosin II intensity for the conditions described in **i**. n = 93 cells (control), n = 71 cells (FL), n = 49 (ΔCC), and n = 41 (ΔaBR) from 3 independent experiments. One-way ANOVA followed by Dunnett's multiple comparisons test; ****$p < 0.0001$ for control vs. FL; **$p = 0.0061$ for control vs. ΔCC; $p = 0.9619$ for control vs. ΔaBR (not significant, n.s.). **k**, Dot plot of EVL cell apical area for the conditions described in **i**. n = 93 cells (control), n = 71 cells (FL), n = 49 (ΔCC), and n = 41 (ΔaBR) from 3 independent experiments. One-way ANOVA followed by Dunnett's multiple comparisons test; ****$p < 0.0001$ for control vs. FL; $p = 0.5849$ for control vs. ΔCC

(not significant, n.s.); p = 0.8620 for control vs. ΔaBR (n.s.). **l**, Dot plot of EVL tissue tension measured at the indicated time points, obtained by micropipette aspiration assay in embryos injected with 25 pg H2B-GFP mRNA (control), 25 pg H2B-GFP and 200 pg (171 amol) wwc1 S643A mRNA (FL), 25 pg H2B-GFP and 142 pg (171 amol) wwc1 S643A ΔCC mRNA (ΔCC), or 25 pg H2B-GFP and 189 pg (171 amol) wwc1 S643A ΔaBR mRNA (ΔaBR) at the 1-cell stage. n = 18 embryos for each condition, except for ΔCC at 6 hpf (n = 17), from 3 independent experiments. One-way ANOVA followed by Dunnett's multiple comparisons test; ****p < 0.0001 for 9 hpf (control) vs. 9 hpf (FL); p = 0.1774 for 9 hpf (control) vs. 9 hpf (ΔCC), n.s.; p = 0.6288 for 9 hpf (control) vs. 9 hpf (ΔaBR), n.s..

Figure 4. Pulling force triggers disassembly of Kibra-associated apical projections

a, Fluorescence images of EVL cells in a Tg*(actb2:Utrophin-mCherry)* embryo, labeling Actin at 6, 7.5, and 9 hpf. Top (apical surface projection of x-y section; upper row) and lateral (x-z section; lower row) views are shown for each time point. Magnified images of the regions demarcated by white squares are shown in the lower-left corner of each image. Scale bar, 20 μm. **b**, Dot plot of mean apical Actin intensity at 6, 7.5, and 9 hpf. n = 304 cells (6 hpf), n = 180 cells (7.5 hpf), and n = 104 cells (8 hpf) from 3 independent experiments. Dunnett's multiple comparisons test; ****p < 0.0001 for 6 hpf vs. 7.5 or 9 hpf. **c**, Electron microscopy images of EVL cells. Apical surfaces of EVL cells at 6 hpf (upper panel) and 9 hpf (lower panel) are shown. Scale bar, 1 μm. **d**, Fluorescence images of EVL cells at 8 hpf in a Tg*(actb2:Utrophin-mCherry)* embryo injected with 25 pg H2A-mCherry mRNA (control YSL) or 25 pg H2A-mCherry plus 150 pg CA-Mypt mRNA (CA-Mypt YSL; to reduce actomyosin contraction within the YSL) into the YSL at 3.3 hpf. Top (apical surface projection of x-y section; upper row) and lateral (x-z section; lower row) views are shown for each condition. Scale bar, 20 μm. **e**, Dot plot of mean apical Actin intensity for the conditions described in **d**. n = 162 cells (control), n = 324 cells (CA-Mypt) from 3 independent experiments. Welch's t-test; ****p < 0.0001. **f**, High-resolution fluorescence images of EVL cells at 6 hpf in a Tg*(actb2:Utrophin-mCherry)* embryo injected with 200 pg mNeonGreen-wwc1 mRNA at the 1-cell stage. mNeonGreen-Kibra (green) and Utrophin-mCherry (magenta) are shown in top (x-y section; left panel) and lateral (x-z section; upper right panel) views. A schematic (lower right panel) illustrates Kibra condensates at the base of the apical projections. Scale bar, 2 μm.

Figure 5. Apical projection disassembly triggers Kibra condensate dissolution

a, Fluorescence images of EVL cell clones injected at the 64-cell stage with 13.1 pg mNeonGreen-wwc1 mRNA (Kibra) or 13.1 pg mNeonGreen-wwc1 plus 9.8 pg CA-Mypt mRNA (to reduce actomyosin contraction) in a Tg*(actb2:mCherry-CAAX)* embryo at 8 hpf. Apical surface projection images of x-y sections for mNeonGreen-Kibra (upper row) and Utrophin-mCherry (lower row) are shown for each condition. Scale bar, 20 μm. **b**,**c**, Dot plot of mean apical Actin intensity (**b**) and mean apical Kibra intensity (**c**) for the conditions described in **a**. n = 84 cells (Kibra), n = 57 cells (Kibra + CA-Mypt) from at least 3 independent experiments. Welch's t-test; ***p = 0.0003 for Kibra vs. Kibra + CA-Mypt (mean apical Actin); ****p < 0.0001 for Kibra vs. Kibra + CA-Mypt (mean apical Kibra). **d**, Scatter plot of mean apical Kibra intensity versus mean apical Actin intensity for the conditions described in **a**. Each dot represents a single cell, expressing mNeonGreen-Kibra (blue) or mNeonGreen-Kibra + CA-Mypt (orange). n = 84 cells (Kibra), n = 57 cells (Kibra + CA-Mypt) from at least 3 independent experiments. Spearman's correlation r; ****p < 0.0001 for both Kibra and Kibra + CA-Mypt samples. **e**, Spatial cross-correlations between Kibra and Actin fluorescence images for the conditions described in **a**. Blue (Kibra) and orange (Kibra + CA-Mypt) lines indicate the mean spatial cross-correlation coefficients with SDs. n = 84 cells (Kibra), n = 57 cells (Kibra + CA-Mypt) from at least 3 independent experiments. **f**, Dot plot of the distances corresponding to the local maxima of the correlation coefficients closest to zero spatial shift for the conditions described in **a**. n = 84 cells (Kibra), n = 57 cells (Kibra + CA-Mypt) from at least 3 independent experiments. Welch's t-test; p = 0.2451 (not significant, n.s.). **g**, Fluorescence images of EVL cells at 7 hpf in Tg*(actb2:Utrophin-mCherry)* embryos, labeling Actin, injected with 200 pg mNeonGreen-wwc1 mRNA at the 1-cell stage to visualize Kibra, and subsequently treated with 0.1% DMSO or 100 μM Endosidin-2 at 4 hpf. Apical surface projection images of x-y sections for Utrophin-mCherry (Actin; upper row) and mNeonGreen-Kibra (lower row) are shown for each condition. Scale bar, 20 μm. **h**,**i**, Dot plot of mean apical Actin intensity (**h**) and mean apical Kibra intensity (**i**) for the conditions described in **g**. n = 141 cells (DMSO), n = 112 cells (Endosidin-2) from 3 independent experiments. Welch's t-test; ****p < 0.0001. **j**, Fluorescence images of EVL cells at 7 hpf in Tg*(actb2:Utrophin-mCherry)* embryos, injected with 200 pg mNeonGreen-wwc1 mRNA at the 1-cell stage to visualize Kibra, and subsequently treated with 0.1% DMSO or 10 μg mL^{-1} Cytochalasin D at 5 hpf in Ringer's solution. Apical surface projection images of x-y sections for Utrophin-mCherry (Actin, upper row) and mNeonGreen-Kibra (lower row) are shown for each condition. Scale bar, 20 μm. **k**,**l**, Dot plot of mean apical Actin intensity (**k**) and mean apical Kibra intensity (**l**) for the conditions described in **p**. n = 56 cells (DMSO), n = 49 cells (Cytochalasin

D) from 3 independent experiments. Welch's t-test; ****p < 0.0001. **m**, A schematic of tissue tension homeostasis governed by apical domain mechanosensation. At 6 hpf (left), Kibra condensates are formed at the base of actin-based apical projections and inhibits aPKC activity. At 9 hpf (right), mechanical stretching of EVL cells triggered by the YSL pulling forces disassemble apical projections and adjacent Kibra condensates, leading to the activation of aPKC and the decrease of cell contractility. This stretch-induced reduction in cell contractility through apical domain mechanosensation buffers the increase in tissue tension, and thus gives rise to tissue tension homeostasis.

Supplementary Figure 1. Contractility of the YSL drives epiboly progression

a, Maximum intensity projection images of Tg*(actb2: Utrophin-mCherry)* embryos at 6, 7, 8, and 9 hpf, labeling F-actin, injected with 25 pg H2B-GFP mRNA (control, top) or 25 pg H2B-GFP plus 150 pg CA-Mypt mRNA (to reduce actomyosin contraction within the YSL, bottom) into YSL at 3.3 hpf. Scale bar, 200 μm. **b**, Line plot of EVL epiboly progression as a function of time during epiboly for the conditions described in **a**. Blue and orange lines indicate control (YSL) and CA-Mypt (YSL) embryos, respectively. Mean ± SD. n = 8 embryos (control YSL), 6 embryos (CA-Mypt YSL) from 3 independent experiments.

Supplementary Figure 2. Pulling force application on the EVL margin dissociates Par3 from the apical domain in EVL cells during epiboly

a, Fluorescence images of EVL cells in an embryo injected with 200 pg pard3ab-EGFP mRNA at the 1-cell stage to visualize Par3 at 6, 7, 8, and 9 hpf. Top (apical surface projection of x-y sections; upper panel) and lateral (x-z section; lower panel) views are shown for each time point. Magnified images of the regions demarcated by white squares are shown in the lower-left corner of each image. Scale bar, 20 μm. **b**, Dot plot of mean apical Par3 intensity at 6, 7, 8, and 9 hpf. n = 116 cells (6 hpf), n = 85 cells (7 hpf), n = 61 cells (8 hpf), n = 38 cells (9 hpf) from 3 independent experiments. One-way ANOVA followed by Dunnett's multiple comparisons test; ****p < 0.0001 for 6 hpf vs. 7, 8, or 9 hpf. **c**, Fluorescence images of EVL cells at 8 hpf in an embryo injected with 200 pg pard3ab-EGFP mRNA at the 1-cell stage to visualize Par3, and injected with 25 pg H2A-mCherry mRNA (control YSL, left panel) or 25 pg H2A-mCherry plus 150 pg CA-Mypt mRNA (CA-Mypt YSL; to reduce actomyosin contraction within the YSL, right panel) into YSL at the 3.3 hpf. Apical surface projection of x-y sections is shown for each condition. Scale bar, 20 μm. **d**, Dot plot of mean apical Par3 intensity for the conditions described in **c**. n = 58 cells (control YSL), n = 141 cells (CA-Mypt YSL) from 3 independent experiments. Welch's t-test; ****p < 0.0001. **e**, Fluorescence images

of EVL cells at 6 hpf in an embryo injected with 200 pg pard3ab-EGFP mRNA (control) or 200 pg pard3ab-EGFP and 50 pg CA-aPKC mRNA (CA-aPKC) at the 1-cell stage. Apical surface projection of x-y sections is shown for each condition. Scale bar, 20 μm. **f**, Dot plot of mean apical Par3 intensity for the conditions described in **e**. n = 196 cells (control), n = 291 cells (CA-aPKC) from 3 independent experiments. Welch's t-test; ***p = 0.0007.

Supplementary Figure 3. EVL cell model schematic and sensitivity analysis

a, Schematic of the minimal vertex model used to describe EVL cell mechanics during epiboly. An EVL cell is represented as a cylinder of initial radius r_0 and height h_0, subject to a lateral pulling stress σ_{ring} from the YSL actomyosin ring. Apical contractility T_a is proportional to the level of apical Myosin II. As σ_{ring} increases, the cell spreads ($r(t)$ increases) and thins ($h(t)$ decreases); the resulting mechanical stretch activates aPKC, which in turn reduces apical Myosin II activity and contractility $T_a(t)$, maintaining homeostatic tissue tension. See Methods for full model description and parameters. **b**, Sensitivity analysis of the vertex model. Each parameter was perturbed by ±30% from its calibrated value independently, and the resulting percentage change in tissue tension (left), apical area (center), and apical Myosin II (right) at t = 9 hpf is shown as a tornado chart. Darker bars indicate +30% perturbation; lighter bars indicate -30% perturbation. The model outputs are most sensitive to τ_M (myosin relaxation timescale) and η (drag coefficient), and least sensitive to k_f (ring ramp rate) and β (aPKC mechanosensitivity), confirming that the qualitative predictions are robust across a broad parameter range.

Supplementary Figure 4. Mutation at a degron motif enhances Kibra expression

a, Alignment of protein sequences surrounding a degron motif in Kibra in *Drosophila melanogaster* (fruit fly), *Homo sapiens* (human), and *Danio rerio* (zebrafish). Amino acids identical across all three species are indicated in an orange background. A key serine residue in the degron motif, a mutation of which to alanine in *Drosophila melanogaster* leads to enhanced Kibra expression level, is indicated in blue. **b**, Cytosolic mNeonGreem-Kibra WT or S643A mutant intensity normalized by cytosolic mCherry intensity in EVL cells at 8 hpf. The embryos were injected with 25 pg mCherry plus 200 pg mNeonGreen-Kibra WT mRNA (WT) or 25 pg mCherry plus 200 pg mNeonGreen-Kibra S643A mRNA at the 1-cell stage. n = 293 cells (WT), n = 219 cells (S643A) from 3 independent experiments. Welch's t-test; ****p < 0.0001.**c**, Dot plot of mean cytosolic Kibra intensity for the conditions described in Figure 3i. n = 71 cells (FL), n = 49 (ΔCC), and n = 41 (ΔaBR) from at least 3 independent experiments.

One-way ANOVA followed by Dunnett's multiple comparisons test; ****$p < 0.0001$ for FL vs. ΔCC; $p = 0.4546$ for FL vs. ΔaBR (not significant, n.s.).

Supplementary Figure 5. Design of the Kibra ΔaBR mutant

a, Alignment of protein sequences surrounding the aPKC-binding region in Kibra in *Drosophila melanogaster* (fruit fly), *Homo sapiens* (human), and *Danio rerio* (zebrafish). Amino acids identical across all three species are highlighted with an orange background. Residues previously shown to be sufficient for aPKC binding by yeast two-hybrid analysis are indicated in red[28,31]. Residues deleted in the ΔaBR mutant in this study are indicated in blue. The region predicted to form an α-helix is underlined in green. **b**, Kibra protein structure predicted by AlphaFold. The predicted α-helix and unstructured regions are indicated in green and blue, respectively.

Supplementary Video 1. Epiboly of embryos with control and DN-aPKC mRNA injections

Time-lapse fluorescence video (10-min time interval) of Tg*(actb2: Utrophin-mCherry)* embryos, corresponding to Figure 2k, with maximum intensity projection. The embryos were injected with 0.05% Phenol Red (control, left) or 300 pg DN-aPKC mRNA (DN-aPKC, right) at the 1-cell stage. Scale bar, 200 μm.

Methods

Zebrafish maintenance and handling

Zebrafish (Danio rerio) were maintained as reported previously[51]. All animal experiments were performed in accordance with the guidelines of the European Union on animal welfare. The following previously reported zebrafish transgenic lines were used in this study: Tg*(actb2:mNeonGreen-zo-1b)*[18], Tg*(actb2:Utrophin-mCherry)*[52], Tg*(actb2: mCherry-CAAX)*[53], Tg*(actb2: Myl12.1-EGFP)*[54], Tg*(actb2: Myl12.1-mCherry)*[54], and Tg*(actb2:Lifeact-EGFP)*[14]. Embryos were collected and kept in E3 medium (4.96 mM NaCl, 0.18 mM KCl, 0.33 mM $CaCl_2$, 0.40 mM $MgCl_2$) at 28.5°C.

Plasmids and mRNA synthesis

The following previously generated plasmids were used in this study: pCS2-H2B-EGFP[55], pCS2-H2A-mCherry[56], pCS2-CA-Mypt[57], pCS2-HA-aPKC (PKCι)-V260F (DN) and pCS2-

HA-aPKC (PKCι)-A122E (CA) (gifts from M. Sonawane, Tata Institute of Fundamental Research, India), pCS2-pard3ab (asip)-EGFP[58], pCS2FA-transposase[59], and pCS2-mCherry. The following plasmids were generated in this study by assembling PCR-amplified inserts with restriction enzyme-digested vectors using the NEBuilder HiFi DNA Assembly Master Mix (E2621L, New England Biolabs), according to the manufacturer's protocol: pCS2-mNeonGreen-Kibra, pCS2-mNeonGreen-Kibra ΔCC, pCS2-mNeonGreen-Kibra ΔaBR, pCS2-mNeonGreen-Kibra S643A, pCS2-mNeonGreen-Kibra S643A ΔCC, pCS2-mNeonGreen-Kibra S643A ΔaBR, pCS2-Kibra S643A, pCS2-Kibra S643A ΔCC, pCS2-Kibra S643A ΔaBR, and pTol2-actb2-HA-mCherry-aPKC (PKCι).

For the cloning of the zebrafish *wwc1* (XM_684183.10) cDNA, encoding Kibra, RNA was purified with TRIzol Reagent (15596026, Invitrogen) from 20 wild-type AB strain embryos at 6 hpf after dechorionation, following the manufacturer's protocol. The extracted RNA was subjected to DNA removal using the DNA-free DNA Removal Kit (AM1906, Invitrogen) and subsequently to cDNA synthesis using the LunaScript RT SuperMix Kit (E3010S, New England Biolabs) by following the manufacturer's protocol. To obtain pCS2-mNeonGreen-Kibra, mNeonGreen with 3 repeats of a SAGG flexible linker sequence at its C-terminus, as well as Kibra cDNA, were amplified by PCR and assembled into the pCS2-Dest2 vector[60]. Compared with the NCBI reference sequence, the Kibra construct used in this study contained the following amino acid substitutions: R400K, E845D, and L876P. Kibra lacking 83-432 amino acids was used as the ΔCC mutant. To design the ΔaBR mutant, the AlphaFold-predicted structure of Kibra was obtained from the AlphaFold Protein Structure Database (UniProt accession: E9QGC4) and visualized using UCSF ChimeraX (Supplementary Fig. 4)[61,62]. Sequence alignment of Kibra proteins from multiple species showed conserved residues surrounding the aPKC-binding region (Supplementary Fig. 4a)[28,31]. Within this conserved region, the C-terminal part was predicted to form an α-helix structure that constitutes part of a helical bundle, whereas the remaining region was predicted to be unstructured (Supplementary Fig. 4b). To minimize the potential disruption of the overall Kibra structure, the ΔaBR mutant was designed by deleting residues 937-984 within the conserved region while retaining the α-helix region. To generate the deletion mutant plasmids, two inserts encoding the upstream and downstream regions of the deletion sites were amplified by PCR and assembled into the pCS2-Dest2 vector. Kibra S643A mutation in a degron motif was introduced into the full-length and deletion mutant plasmids by site-directed mutagenesis to generate pCS2-mNeonGreen-Kibra S643A, pCS2-mNeonGreen-Kibra S643A ΔCC, and pCS2-mNeonGreen-Kibra S643A ΔaBR plasmids. For the generation of pCS2-Kibra S643A, pCS2-Kibra S643A ΔCC, and pCS2-Kibra

S643A ΔaBR, the corresponding Kibra sequences were amplified from the mNeonGreen-tagged Kibra S643A constructs and inserted into the pCS2-Dest2 vector.

For the generation of pTol2-actb2:mCherry-HA-aPKC (PKCι), the HA-aPKC (PKCι), a fragment amplified from pCS2-HA-aPKC (PKCι) (a gift from M. Sonawane, Tata Institute of Fundamental Research, India) and the mCherry fragment were assembled into the pCS2-Dest2 vector to obtain pCS2-mCherry-HA-aPKC (PKCι). The PCR-amplified mCherry-HA-aPKC (PKCι) fragment from the pCS2-mCherry-HA-aPKC (PKCι) plasmid and the beta-actin promoter fragment from p5E-bactin2[59] were assembled into the pDestTol2pA2 vector[59] to obtain pTol2-actb2:mCherry-HA-aPKC (PKCι).

mRNAs were synthesized with mMESSAGE mMACHINE SP6 Transcription Kit (AM1340, Invitrogen), following the manufacturer's protocol, by using the above-mentioned pCS2 plasmids as a template after the digestion with NotI enzyme. Synthesized mRNAs were diluted for injection according to the amounts described in the figure legends. To visualize the injection droplet, Phenol red (P-5530, Sigma-Aldrich; final 0.05%) was added to the injection solution.

Reagents

The following reagents were used in this study: dextran fluorescein and biotin 10,000 MW (D7178, Invitrogen) dissolved in Nuclease-Free Water (AM9937, Invitrogen), dextran Alexa Fluor 594 10,000 MW (D22913, Invitrogen) dissolved in Nuclease-Free Water, Endosidin-2 (HY-120821, MedChem Express) dissolved in dimethyl sulfoxide (DMSO; D8418, Sigma-Aldric), and Cytochalasin D (C8273, Sigma-Aldrich) dissolved in DMSO. For the treatment with Cytochalasin D, the embryos were incubated in Ringer's solution (isotonic medium; 116 mM NaCl, 2.9 mM KCl, 1.8 mM $CaCl_2$, 5 mM HEPES, pH 7.4) containing 10 μg mL^{-1} Cytochalasin D to avoid osmotic cell swelling and resultant cell/tissue rupturing.

Embryo microinjections

Injection needles were prepared by pulling glass capillaries (BS4 30-0020, Harvard Apparatus) with a Flaming/Brown Micropipette Puller (P-97, Sutter Instrument). The needle filled with injection solution was connected to a Pneumatic PicoPump microinjector (PV 820 or PV 830, World Precision Instruments), and then the needle tip was cut to adjust the injection droplet size.

For the injection at the 1-cell stage, the droplet diameter was adjusted to 100 μm, with a droplet volume of approximately 0.5 nL. mRNA solutions were injected into the embryos twice, without dechorionation, to achieve a total volume of approximately 1 nL.

For the 64-cell stage injection, the droplet diameter was set to 50 μm, with an approximate total volume of 65 pL. Embryos at 2 hpf were dechorionated, and a single blastomere at the animal pole was injected with mRNA solutions only once (approximately 65 pL total volume).

For the injection into the YSL, the droplet diameter was adjusted to 100 μm. Embryos at 3.3 hpf were dechorionated, and each side of the YSL was injected once with mRNA solutions.

Establishment of Tg*(actb2: mCherry-HA-prkci)*

Wild-type embryos were injected with 12.5 pg pTol2-actb2:mCherry-HA-aPKC (PKCι) plasmid and 12.5 pg Tol2 transposase mRNA at the 1-cell stage. Embryos exhibiting bright and relatively uniform mCherry fluorescence were selected and raised to adulthood as F0 founders. F1 embryos were obtained by crossing F0 founders to wild-type fish, and F1 embryos with bright mCherry fluorescence were raised to adulthood. F2 embryos obtained by outcrossing F1 females to wild-type males were used for experiments.

Sample preparation and time-lapse imaging

For fluorescence confocal microscopy, embryos were mounted in 0.5% Low Melting Point Agarose (16520-100, Invitrogen) in E3, unless otherwise noted, in a 4-chamber 35 mm glass-bottom dish with #1.5 cover glass (D35C4-20-1.5-N, Cellvis). For lateral-view imaging of developing embryos and imaging of EVL cells at the animal pole, the embryos were oriented with the lateral side or the animal pole facing downward toward the glass bottom of the dishes, respectively.

Low-magnification imaging of whole embryos was performed using Zeiss LSM 900 or LSM 980 inverted confocal microscopes equipped with a Plan-Apochromat 10x/0.45 dry objective. Standard confocal imaging of EVL cells was performed using Zeiss LSM 900 inverted confocal microscopes equipped with a Plan-Apochromat 40x/1.2 water-immersion objective. The incubation temperature was set to 28.5°C during imaging. For high-magnification imaging of mNeonGreen-Kibra and Utrohin-mCherry, images were acquired using Airyscan 2 detection on the Zeiss LSM 980 microscope and subsequently processed using ZEN software (Carl Zeiss).

Micropipette aspiration assay

The micropipette aspiration assay was performed as previously described[19], with some modifications. Embryos were placed on a layer of 3% methyl cellulose (M6385, Sigma-Aldrich) in E3 covering the glass bottom of a 50-mm glass-bottom dish with #1.5 cover glass (P50G-1.5-14-F, MatTek). Embryos were imaged using a Leica Stellaris 5 confocal microscope equipped with an HC PL APO 20x/0.75 CS2 objective. A blunt-ended glass micropipette with an inner diameter of 60 μm and a 30° bend 1 mm away from the tip (SRP-60Z-30L, Sunlight Medical) was connected to a Microfluidic Flow Control system (Fluigent), with a height-controlled reservoir filled with E3 placed in between. To calibrate the pressure control, mechanically dissociated embryos were aspirated by applying negative pressure of 200 Pa, and the height of the reservoir was then adjusted until the aspiration flow is stopped.

The micropipette was positioned at EVL cells at the animal pole of the embryos using a TransferMan 4r micromanipulator (Eppendorf). Negative pressure was applied in stepwise increments of 5 Pa to aspirate the EVL until the aspirated EVL formed a hemisphere with a radius corresponding to that of the micropipette, typically occurring within 3 min. The magnitude of the pressure at this point was defined as the critical pressure (P_c). The EVL tension along the plane of the tissue was calculated using the Young–Laplace equation: $\gamma = P_c/[2(1/R_p - 1/R_e)]$, where γ is the tissue tension, P_c is the critical pressure, and R_p and R_e are the radii of the micropipette and embryo, respectively. An estimated embryo radius of 375 μm was used to calculate the tissue tension.

Transmission electron microscopy

Wild-type embryos were dechorionated and fixed at 6 and 9 hpf in PBS containing 2.5% glutaraldehyde (E16220, Science Services) and 4% paraformaldehyde (E15714, Science Services) for 2 h at room temperature, followed by overnight incubation at 4°C. Embryos were subsequently washed three times in PBS and processed using a microwave-assisted heavy metal staining protocol (rOTO fixation)[63] with a PELCO BioWave Pro+ Microwave Tissue Processing System (AGL4376, Agar Scientific) operated under vacuum conditions.

Embryos were first incubated in a solution containing 2% osmium tetroxide (OsO_4; E19110, Science Services) and 1.5% potassium ferrocyanide (P9387, Sigma-Aldrich) in 120 mM phosphate buffer (PB; pH7.4) using six cycles of 2 min on/2 min off at 100 W under vacuum. Samples were then washed three times in Milli-Q water (Millipore) for 40 s each at 250 W. This was followed by incubation in filtered 1% thiocarbohydrazide (TCH; 88535-5G, Sigma-

Aldrich) under identical microwave/vacuum conditions (100 W, six cycles of 2 min on/2 min off), followed again by three washes in Milli-Q water.

A second osmium staining step was performed using 2% aqueous OsO_4 under the same microwave-assisted vacuum conditions. After washing as described above, embryos were incubated in 1% aqueous uranyl acetate (77870.02, AL-Labortechnik & Diagnostik GmbH) at 100 W under vacuum for six cycles of 2 min on/2 min off, followed by additional washes in Milli-Q water. Samples were then incubated in lead aspartate solution (prepared from L-aspartic acid, A8949, Sigma-Aldrich, and lead nitrate, 228621, Sigma-Aldrich) at 60°C for 30 min and subsequently washed again in Milli-Q water.

Embryos were dehydrated through a graded ethanol series (50%, 70%, 90%, and twice in 100% ethanol; 32221-2.5L-GL, Bartelt), with each step performed for 40 s at 250 W. Samples were then infiltrated with increasing concentrations of hard Durcupan™ ACM resin (44611, 44612, 44613, 44614, Sigma-Aldrich) in ethanol (25%, 50%, 75%, and twice in 100%) for 3 min each at 250 W under vacuum. Finally, embryos were embedded in BEEM capsules (E70020-B, Science Services) and polymerized at 60°C for 3 days.

Ultrathin sections (70 nm) were prepared using a 4 mm Ultra 35° diamond knife (DU3540, Science Services) mounted on an ultramicrotome (EM UC7, Leica Microsystems) and collected on formvar-coated copper slot grids. Imaging was performed using a Tecnai 10 transmission electron microscope (FEI/Thermo Fisher Scientific) operated at 80 kV and equipped with an OSIS Megaview III camera (Emsis).

Analysis of epiboly progression

Maximum-intensity projections of whole-embryo z-stack images were used to analyze epiboly progression. Epiboly progression was quantified as the percentage of the animal–vegetal axis covered by the EVL, calculated by dividing the distance from the animal pole to the EVL margin by the total distance between the animal and vegetal poles and multiplying by 100.

EVL surface projection and quantification

For the analysis of EVL cell apical area, z-stack images of EVL cells at the animal pole were processed using a custom MATLAB script to obtain apical surface projection images. Briefly, the surface position at each xy-coordinate was determined from the z-stack images after Gaussian blurring by identifying the first z-plane in which the fluorescence intensity exceeded a predefined threshold. For each xy-coordinate, maximum-intensity projection was performed

over a defined z-range around the detected surface position. EVL cells in the surface projection images were segmented using Cellpose3 with the cyto3 model[64,65], followed by manual correction. Cells located at the margin of the images were excluded from the following analysis. The segmented cells were analyzed in Fiji to measure the apical area of each cell[66].

Mean apical intensities of Actin markers (Lifeact and Utrophin), Myosin II, Kibra, and Par3 were quantified from the apical surface projection images using Fiji. To exclude junctional signals, each segmented cell was eroded before measurement. Fluorescence signals within the eroded apical region were identified by thresholding. Background subtraction was applied before intensity measurement for Kibra, Myosin II, and Par3 to reduce background signals. For each cell, the total intensity of the thresholded pixels within the eroded apical region was measured and divided by the corresponding area to calculate the mean apical intensity. For Kibra and Par3, the mean apical intensity was further normalized to the corresponding cytoplasmic fluorescence intensity measured adjacent to the nucleus in each cell to correct for differences in expression levels. For Kibra, cells with cytoplasmic fluorescence intensity below a predefined threshold were excluded from the analysis to remove cells with little or no detectable expression.

Cell proliferation analysis

For the analysis of the time-dependent changes in cell proliferation rate, time-lapse z-stack images of EVL cells in Tg*(actb2:mNeonGreen-zo-1b)* embryos were subjected to apical surface projection as described above. EVL cells were segmented using Cellpose3, followed by manual correction, and the number of cells in each image was quantified. Embryos with insufficient fluorescence signal for reliable cell segmentation were excluded from the analysis. Cell proliferation events were counted manually in the apical surface projection images. Cells located at the margin of the images were excluded from the analysis. Cell proliferation events were binned into 30-min time windows, and the number of cell proliferation events in each time window was divided by the number of cells at the initial time point of the time window and by 30 to calculate the cell proliferation rate per cell per minute.

Cross-correlation analysis

Spatial cross-correlation between Actin (Utrophin) and Kibra signals was quantified from apical surface projection images and corresponding cell segmentation masks described above using a custom MATLAB script, after background subtraction and median filtering. For each cell, the segmented region of interest (ROI) was morphologically eroded to exclude junctional

pixels. Within each eroded ROI, Actin and Kibra fluorescence intensities were mean-centered by subtracting the average intensity of the respective channel, while pixel intensities outside the ROI were set to zero. The spatial cross-correlation coefficient $r(\Delta x,\Delta y)$ between the two-dimensional Actin and Kibra intensity distributions was then calculated as follows:

$$r(\Delta x, \Delta y) = \frac{\Sigma_{x,y} f(x,y) g(x + \Delta x, y + \Delta y)}{\sqrt{\Sigma_{x,y} f(x,y)^2 \, \Sigma_{x,y} g(x,y)^2}}$$

where f(x,y) and g(x,y) represent the mean-centered Actin and Kibra fluorescence intensities, respectively. The resulting cross-correlation maps were radially averaged around the zero-displacement position to obtain distance-dependent cross-correlation profiles. The peak distance was defined as the distances from the zero-displacement position to the nearest local maximum of the radially averaged cross-correlation profile.

Statistical Analysis

Statistical analyses were performed with GraphPad Prism 7 or 10 software (GraphPad Software). No statistical analysis was used to predetermine the sample size. The sample sizes, statistical tests, and p-values are indicated in the figure legends. All statistical tests were two-sided. p-values were classified as follows: $*p < 0.05$, $**p < 0.01$, $***p < 0.001$, $****p < 0.0001$, and n.s. (not significant, i.e., $p \geq 0.05$).

Minimal vertex model of EVL cell mechanics.

We represent each EVL cell as a prism with an apical face of radius $r(t)$ and height $h(t)$. Cell volume is assumed to be conserved and hence we fix V throughout the simulation window. This links height to radius through $h = V/\pi r^2$ (we neglect geometrical prefactors linked to the exact shape of the apical face, as they only serve to rescale relative tensions).

The mechanical energy of the cell is written as a sum over its faces (Fig. 1j). T_a is assigned to the apical face. The basal face is assumed to be under passive tension only; for simplicity this is taken to be small relative to apical contractility, so the dominant active contribution to lateral force balance comes from the apical face alone. The lateral face (area $2\pi r \cdot h$) carries the passive lateral junction tension Γ_l. For a prism geometry, the apical and basal faces both contribute to the horizontal force balance on the cell radius; absorbing the basal passive contribution into an effective rescaling of the junction tension, the mechanical energy takes the form:

$$E = 2T_a \cdot \pi r^2 + 2\pi\Gamma_l \cdot r \cdot h$$

where the factor of 2 in the first term captures the geometric contribution of both apical and basal faces to the lateral force balance, and does not imply equal myosin levels on both faces. Changing this prefactor would only rescale the inferred value of maximum apical tension T_a without affecting any qualitative prediction of the model.

Differentiating with respect to apical area $A = \pi r^2$ at constant volume and substituting the volume constraint gives the tissue tension γ, the quantity directly measured by micropipette aspiration via the Young–Laplace relation:

$$\gamma = 2T_a - \Gamma_l \cdot h/r$$

The first term, $2T_a$, is the active contractile resistance to spreading. The second term, $\Gamma_l \cdot h/r$, is purely geometric: as cells spread and flatten, h/r falls, and this term decreases, partially preventing further spreading. Crucially, if T_a is held constant while r grows, γ rises passively. Such tension increase is characteristic of any elastic material with reference length, something that the mechanosensitive circuit must counteract to achieve tension homeostasis.

The YSL actomyosin ring exerts a distributed radial pulling force σ_{ring} per unit length on the EVL margin. In the overdamped limit appropriate for epithelial monolayers, the horizontal force balance on the apical radius is:

$$\eta\, dr/dt = \sigma_{ring}(t) - \gamma$$

where η is the effective lateral drag. We model the ring force as a linear ramp in time,

$$\sigma_{ring}(t) = \sigma_0 + k_f \cdot t$$

where t is minutes from 6 hpf. This is the simplest assumption consistent with the gradual acceleration of spreading, as well as of actomyosin tensions in the YSL, previously measured experimentally[14], and the initial value σ_0 and slope k_f are calibrated per condition.

Apical junction tension T_a is taken to be proportional to apical Myosin II level M, reflecting the well-established role of Myosin II in driving actomyosin contractility[9,10]. To capture the possible non-linear coupling between T_a and myosin, we use a Hill function to relate myosin level M to tension:

$$T_a = \Sigma \frac{M^n}{(M^n + M_H{}^n)}$$

where Σ is the maximum junction tension, M_H is the myosin saturation level, and $n = 0.5$. The exponent $n < 1$ gives a concave (sublinear) response: T_a decreases more slowly than M, so a moderate Myosin drop produces substantial tension relief. This is what makes homeostasis achievable at biologically realistic parameter values. Σ is calibrated so that γ at $t = 6$ hpf matches the measured EVL tension γ_0.

The central mechanosensitive ingredient of the model is that Myosin II levels are not fixed, but relaxes toward a strain-dependent equilibrium $M = M_{eq}$. This equilibrium myosin level decreases with increasing apical strain, with time delay τ_M:

$$\tau_M \frac{dM_{eq}}{dt} = M_H/(1 + \beta\varepsilon) - M_{eq}$$

Here $\varepsilon = \pi r^2/A_0 - 1$ is the fractional apical strain relative to the initial cell area A_0. The parameter β sets the aPKC mechanosensitivity. As cells spread, ε grows, M_{eq} falls, and Myosin follows with a lag set by τ_M. This relaxation term can be interpreted as a coarse-grained representation of a mechanosensitive feedback circuit in which apical stretch reduces Myosin activity through an intermediate signaling cascade, with τ_M capturing the finite delay of that response. This interpretation is consistent with the view that individual signaling steps may be fast while the adaptation of the mechanical set-point is governed by the cascade as a whole[26]. We also note that a decrease of T_a, at constant lateral tension and constant volume, means effectively that the preferred spreading area of a given cell increases over time. In previous works[67] which modelled the EVL apical area via a 2D vertex model, an increase of preferred area A_0 was inputted in the model (to concentrate on the role of keratin upregulation), which our current mechanosensitive model can naturally capture.

Simulation conditions and Parameter mapping

With this setup, each experimental condition naturally maps to a specific parameter choice. For control, the ring force slightly exceeds tissue tension at $t = 6$ hpf ($\sigma_0 = \gamma_0 + \Delta$), placing cells just above mechanical equilibrium so that spreading begins immediately. For CA-Mypt (YSL), reduced YSL contractility places the ring force at equilibrium with tissue tension at $t = 6$ hpf ($\sigma_0 = \gamma_0$), capturing the slower and delayed spreading; because CA-Mypt acts exclusively within the YSL, the EVL mechanosensitive circuit is otherwise unchanged. For DN-aPKC, Myosin II is frozen at its maximum value M_H throughout, reflecting the absence of aPKC-mediated mechanosensitive downregulation. Because DN-aPKC embryos have sustained elevated myosin for approximately six hours prior to the model window, the junction tension

parameter Σ_{DN} is recalibrated to match the elevated surface tension measured at t = 6 hpf; the ring force is set equal to the control value for the sake of simplicity. For DN-aPKC + CA-Mypt (YSL), the ring force follows the CA-Mypt condition ($\sigma_0 = \gamma_0$) and Myosin II is frozen at M_H as in DN-aPKC; since CA-Mypt acts only within the YSL, EVL junction tension remains Σ_{DN}. No additional parameters are tuned for this combined condition.

Two parameters are fixed directly from data: γ_0 from micropipette aspiration measurements at t = 6 hpf, and Σ from the tension formula evaluated at t = 6 hpf with $M = M_H$. The remaining parameters were calibrated sequentially: k_f and η to match control and DN-aPKC apical area at t = 9 hpf; β and τ_M to reproduce qualitative behavior of the measured myosin decrease from 6.32 to 2.20 A.U. between t = 6 and 9 hpf; and Δ to match the control spreading rate. Parameters for CA-Mypt and DN + CA-Mypt were not subsequently adjusted, as those conditions are predictions of the calibrated model. All outputs are normalized to control at t = 6 hpf to illustrate qualitative trends.

Numerical implementation and sensitivity analysis.

The ODEs for $r(t)$ and $M(t)$ were integrated with a fourth-order Runge–Kutta scheme (time step 0.5 min) in Python 3 (NumPy; Matplotlib for figures). To assess robustness, we varied each of five parameters ($\beta, k_f, \Delta, \tau_M, \eta$) independently by ±30% from its nominal value and recorded the percentage change in tissue tension, apical Myosin, and apical area at t = 9 hpf (Supplementary Fig. 3b, tornado chart). τ_M dominates tension (+9.3%) and Myosin (+17.6%) output; η dominates area kinetics (+24.9%); β and k_f produce modest effects of 12% or less on any output. This confirms that tissue tension homeostasis is a robust consequence of the circuit topology rather than of precisely tuned parameter values. All model parameters are listed in Table 1.

Table 1 (EVL Cell Model Parameters)

Parameter	Symbol	Value	How determined
Lateral drag	η	14.0 nN·min/μm	Calibrated to Control area timecourse

Parameter	Symbol	Value	How determined
Ring ramp rate	k_f	0.003 nN/µm/min	Calibrated to control area at t = 9 hpf
Ring offset (Control)	Δ	0.40 nN/µm	Calibrated to control spreading rate
aPKC mechanosensitivity	β	12	Calibrated to control Myosin drop
Timescale for feedback on MyoII	τ_M	90 min	Calibrated to Myosin decrease timescale
Hill exponent	n	0.50	Chosen for concave Myosin–tension coupling
Myosin saturation	M_H	0.80	Sets Myosin scale (model units)
Lateral junction tension	Γ_l	1.50 nN/µm	Calibrated from geometry and tension at t = 6 hpf
EVL tension at t = 6 hpf	γ_0	0.983 nN/µm	Directly from micropipette aspiration
Initial cell radius	r_0	16 µm	Data

Code availability

The MATLAB code for image analysis, and the full model code, including all parameter values and condition-specific settings, are available on GitHub at https://github.com/uday2607/EVL-tension-homeostasis.git.

Acknowledgements

We thank all members of the Heisenberg group for discussion and feedback on the manuscript, and the Imaging and Optics Facility, the Lab Support Facility and the Electron Microscopy

Facility of the Institute of Science and Technology Austria (ISTA) for their continued support. We are grateful to M. Sonawane (Tata Institute of Fundamental Research, India) for providing the pCS2-HA-aPKC (PKCι)-V260F (DN) and pCS2-HA-aPKC (PKCι)-A122E (CA) plasmids, and to I. Mayer for the discussion. Molecular graphics and analyses were performed with UCSF ChimeraX, developed by the Resource for Biocomputing, Visualization, and Informatics at the University of California, San Francisco, with support from National Institutes of Health R01-GM129325 and the Office of Cyber Infrastructure and Computational Biology, National Institute of Allergy and Infectious Diseases. This research was funded in whole or in part by the Austrian Science Fund (FWF; grant no. PAT5044023) to C.-P.H., and by a JSPS Overseas Research Fellowship and an EMBO Postdoctoral Fellowship (ALTF 16-2022) to N.H.

Author contributions

Conceptualization, N.H. T.K., and C.-P.H.; Methodology, N.H., T.K., U.R.G., É.H., and C.-P.H.; Investigation, N.H., T.K., U.R.G.; Resources, N.H., T.K., and C.-P.H.; Formal analysis, N.H., U.R.G.; Writing – original draft, N.H., U.R.G, É.H., and C.-P.H.; Writing – review & editing, N.H., T.K., U.R.G, É.H., and C.-P.H.; Funding acquisition, N.H. and C.-P.H.

Competing interests

The authors declare no competing interests.

References

1. Balaji, R., Weichselberger, V. & Classen, A.-K. Response of Drosophila epithelial cell and tissue shape to external forces in vivo. *Development* **146**, dev171256 (2019).

2. Sui, L. & Dahmann, C. Wingless counteracts epithelial folding by increasing mechanical tension at basal cell edges in Drosophila. *Development* **147**, dev184713 (2020).

3. Naganathan, S. R., Popović, M. & Oates, A. C. Left–right symmetry of zebrafish embryos requires somite surface tension. *Nature* **605**, 516–521 (2022).

4. Porazinski, S. *et al.* YAP is essential for tissue tension to ensure vertebrate 3D body shape. *Nature* **521**, 217–221 (2015).

5. Osswald, M. *et al.* aPKC regulates apical constriction to prevent tissue rupture in the Drosophila follicular epithelium. *Curr. Biol.* **32**, 4411-4427.e8 (2022).

6. Campinho, P. *et al.* Tension-oriented cell divisions limit anisotropic tissue tension in epithelial spreading during zebrafish epiboly. *Nat. Cell Biol.* **15**, 1405–1414 (2013).

7. Pérez-González, C. *et al.* Active wetting of epithelial tissues. *Nat. Phys.* **15**, 79–88 (2019).

8. Chan, C. J. *et al.* Hydraulic control of mammalian embryo size and cell fate. *Nature* **571**, 112–116 (2019).

9. Murrell, M., Oakes, P. W., Lenz, M. & Gardel, M. L. Forcing cells into shape: the mechanics of actomyosin contractility. *Nat. Rev. Mol. Cell Biol.* **16**, 486–498 (2015).

10. Sawyer, J. M. *et al.* Apical constriction: a cell shape change that can drive morphogenesis. *Dev. Biol.* **341**, 5–19 (2010).

11. Maître, J.-L. *et al.* Asymmetric division of contractile domains couples cell positioning and fate specification. *Nature* **536**, 344–348 (2016).

12. Raman, R. *et al.* aPKC regulates apical localization of Lgl to restrict elongation of microridges in developing zebrafish epidermis. *Nat. Commun.* **7**, 11643 (2016).

13. Ishiuchi, T. & Takeichi, M. Willin and Par3 cooperatively regulate epithelial apical constriction through aPKC-mediated ROCK phosphorylation. *Nat. Cell Biol.* **13**, 860–866 (2011).

14. Behrndt, M. *et al.* Forces driving epithelial spreading in zebrafish gastrulation. *Science* **338**, 257–260 (2012).

15. Kimmel, C. B., Ballard, W. W., Kimmel, S. R., Ullmann, B. & Schilling, T. F. Stages of embryonic development of the zebrafish. *Dev. Dyn.* **203**, 253–310 (1995).

16. Morita, H. *et al.* The physical basis of coordinated tissue spreading in zebrafish gastrulation. *Dev. Cell* **40**, 354-366.e4 (2017).

17. Kane, D. A., Warga, R. M. & Kimmel, C. B. Mitotic domains in the early embryo of the zebrafish. *Nature* **360**, 735–737 (1992).

18. Schwayer, C. *et al.* Mechanosensation of tight junctions depends on ZO-1 phase separation and flow. *Cell* **179**, 937-952.e18 (2019).

19. Guevorkian, K. & Maitre, J.−L. Micropipette aspiration: a unique tool for exploring cell and tissue mechanics in vivo. *Methods Cell Biol.* **139**, 187–201 (2017).

20. Fletcher, A. G., Osterfield, M., Baker, R. E. & Shvartsman, S. Y. Vertex models of epithelial morphogenesis. *Biophys. J.* **106**, 2291–2304 (2014).

21. Nagai, T. & Honda, H. A dynamic cell model for the formation of epithelial tissues. *Philos. Mag. B* **81**, 699–719 (2001).

22. Alt, S., Ganguly, P. & Salbreux, G. Vertex models: from cell mechanics to tissue morphogenesis. *Philos. Trans. R. Soc. Lond. B. Biol. Sci.* **372**, 20150520 (2017).

23. Latorre, E. *et al.* Active superelasticity in three-dimensional epithelia of controlled shape. *Nature* **563**, 203–208 (2018).

24. Soriano, E. V. *et al.* aPKC inhibition by Par3 CR3 flanking regions controls substrate access and underpins apical-junctional polarization. *Dev. Cell* **38**, 384–398 (2016).

25. Morais-de-Sá, E., Mirouse, V. & St Johnston, D. aPKC phosphorylation of Bazooka defines the apical/lateral border in Drosophila epithelial cells. *Cell* **141**, 509–523 (2010).

26. Boocock, D., Hino, N., Ruzickova, N., Hirashima, T. & Hannezo, E. Theory of mechanochemical patterning and optimal migration in cell monolayers. *Nat. Phys.* **17**, 267–274 (2021).

27. Hannezo, E., Prost, J. & Joanny, J.-F. Theory of epithelial sheet morphology in three dimensions. *Proc. Natl. Acad. Sci. USA* **111**, 27–32 (2014).

28. Yoshihama, Y. *et al.* KIBRA suppresses apical exocytosis through inhibition of aPKC kinase activity in epithelial cells. *Curr. Biol.* **21**, 705–711 (2011).

29. Wang, L. *et al.* Multiphase coalescence mediates Hippo pathway activation. *Cell* **185**, 4376-4393.e18 (2022).

30. Bonello, T. T. *et al.* Phase separation of Hippo signalling complexes. *EMBO J.* **42**, e112863 (2023).

31. Büther, K., Plaas, C., Barnekow, A. & Kremerskothen, J. KIBRA is a novel substrate for protein kinase Cζ. *Biochem. Biophys. Res. Commun.* **317**, 703–707 (2004).

32. Tokamov, S. A., Su, T., Ullyot, A. & Fehon, R. G. Negative feedback couples Hippo pathway activation with Kibra degradation independent of Yorkie-mediated transcription. *eLife* **10**, e62326 (2021).

33. Tokamov, S. A. *et al.* Apical polarity and actomyosin dynamics control Kibra subcellular localization and function in Drosophila Hippo signaling. *Dev. Cell* **58**, 1864-1879.e4 (2023).

34. Pinto, C. S. *et al.* Microridges are apical epithelial projections formed of F-actin networks that organize the glycan layer. *Sci. Rep.* **9**, 12191 (2019).

35. van Loon, A. P., Erofeev, I. S., Goryachev, A. B. & Sagasti, A. Stochastic contraction of myosin minifilaments drives evolution of microridge protrusion patterns in epithelial cells. *Mol. Biol. Cell* **32**, 1501–1513 (2021).

36. Figard, L., Wang, M., Zheng, L., Golding, I. & Sokac, A. M. Membrane supply and demand regulates F-actin in a cell surface reservoir. *Dev. Cell* **37**, 267–278 (2016).

37. Khalilgharibi, N. *et al.* Stress relaxation in epithelial monolayers is controlled by the actomyosin cortex. *Nat. Phys.* **15**, 839–847 (2019).

38. Fletcher, G. C. *et al.* Mechanical strain regulates the Hippo pathway in Drosophila. *Development* **145**, dev159467 (2018).

39. Mooseker, M. S. Organization, chemistry, and assembly of the cytoskeletal apparatus of the intestinal brush border. *Annu. Rev. Cell Dev. Biol.* **1**, 209–241 (1985).

40. Fletcher, G. C. *et al.* The spectrin cytoskeleton regulates the Hippo signalling pathway. *EMBO J.* **34**, 940–954 (2015).

41. Deng, H. *et al.* Spectrin regulates Hippo signaling by modulating cortical actomyosin activity. *eLife* **4**, e06567 (2015).

42. Mylvaganam, S. *et al.* The spectrin cytoskeleton integrates endothelial mechanoresponses. *Nat. Cell Biol.* **24**, 1226–1238 (2022).

43. Duan, R. *et al.* Spectrin is a mechanoresponsive protein shaping fusogenic synapse architecture during myoblast fusion. *Nat. Cell Biol.* **20**, 688–698 (2018).

44. Baumgartner, R., Poernbacher, I., Buser, N., Hafen, E. & Stocker, H. The WW domain protein Kibra acts upstream of Hippo in Drosophila. *Dev. Cell* **18**, 309–316 (2010).

45. Genevet, A., Wehr, M. C., Brain, R., Thompson, B. J. & Tapon, N. Kibra is a regulator of the Salvador/Warts/Hippo signaling network. *Dev. Cell* **18**, 300–308 (2010).

46. Acharya, B. R. *et al.* A mechanosensitive RhoA pathway that protects epithelia against acute tensile stress. *Dev. Cell* **47**, 439-452.e6 (2018).

47. Tan, P. Y. & Zaidel-Bar, R. Transient membrane localization of SPV-1 drives cyclical actomyosin contractions in the C. elegans spermatheca. *Curr. Biol.* **25**, 141–151 (2015).

48. Casares, L. *et al.* Hydraulic fracture during epithelial stretching. *Nat. Mater.* **14**, 343–351 (2015).

49. Tajvidi Safa, B. *et al.* Sustained strain applied at high rates drives dynamic tensioning in epithelial cells. *Commun. Biol.* **8**, 843 (2025).

50. Doerflinger, H. *et al.* An aPKC rheostat induces apical contraction in response to epithelial stretching. Preprint at https://doi.org/10.64898/2026.05.05.722904 (2026).

51. Westerfield, M. The zebrafish book: a guide for the laboratory use of zebrafish (Danio rerio) 5th edn. *Univ. of Oregon Press, Eugene* (2007).

52. Krens, S. F. G. *et al.* Interstitial fluid osmolarity modulates the action of differential tissue surface tension in progenitor cell segregation during gastrulation. *Development* **144**, 1798–1806 (2017).

53. Tavano, S. *et al.* BMP-dependent patterning of ectoderm tissue material properties modulates lateral mesendoderm cell migration during early zebrafish gastrulation. *Cell Rep.* **44**, 115387 (2025).

54. Maître, J.-L. *et al.* Adhesion functions in cell sorting by mechanically coupling the cortices of adhering cells. *Science* **338**, 253–256 (2012).

55. Keller, P. J., Schmidt, A. D., Wittbrodt, J. & Stelzer, E. H. K. Reconstruction of zebrafish early embryonic development by scanned light sheet microscopy. *Science* **322**, 1065–1069 (2008).

56. Arboleda-Estudillo, Y. *et al.* Movement directionality in collective migration of germ layer progenitors. *Curr. Biol.* **20**, 161–169 (2010).

57. Smutny, M. *et al.* Friction forces position the neural anlage. *Nat. Cell Biol.* **19**, 306–317 (2017).

58. Geldmacher-Voss, B., Reugels, A. M., Pauls, S. & Campos-Ortega, J. A. A 90° rotation of the mitotic spindle changes the orientation of mitoses of zebrafish neuroepithelial cells. *Development* **130**, 3767–3780 (2003).

59. Kwan, K. M. *et al.* The Tol2kit: a multisite gateway-based construction kit for Tol2 transposon transgenesis constructs. *Dev. Dyn.* **236**, 3088–3099 (2007).

60. Villefranc, J. A., Amigo, J. & Lawson, N. D. Gateway compatible vectors for analysis of gene function in the zebrafish. *Dev. Dyn.* **236**, 3077–3087 (2007).

61. Pettersen, E. F. *et al.* UCSF ChimeraX: Structure visualization for researchers, educators, and developers. *Protein Sci.* **30**, 70–82 (2021).

62. Bertoni, D. *et al.* AlphaFold Protein Structure Database 2025: a redesigned interface and updated structural coverage. *Nucleic Acids Res.* **54**, D358–D362 (2026).

63. Deerinck, T. *et al.* NCMIR methods for 3D EM: a new protocol for preparation of biological specimens for serial block face scanning electron microscopy. https://www.semanticscholar.org/paper/NCMIR-methods-for-3D-EM%3A-a-new-protocol-for-of-for-Deerinck-Bushong/49ebf43a6645985c3fb7d9e1336358b5b6d7cb8a (2010).

64. Stringer, C., Wang, T., Michaelos, M. & Pachitariu, M. Cellpose: a generalist algorithm for cellular segmentation. *Nat. Methods* **18**, 100–106 (2021).

65. Stringer, C. & Pachitariu, M. Cellpose3: one-click image restoration for improved cellular segmentation. *Nat. Methods* **22**, 592–599 (2025).

66. Schindelin, J. *et al.* Fiji: an open-source platform for biological-image analysis. *Nat. Methods* **9**, 676–682 (2012).

67. Naik, S. *et al.* Keratins coordinate tissue spreading by balancing spreading forces with tissue material properties. *Nat. Commun.* https://doi.org/10.1038/s41467-026-72366-z (2026).

Figure 1

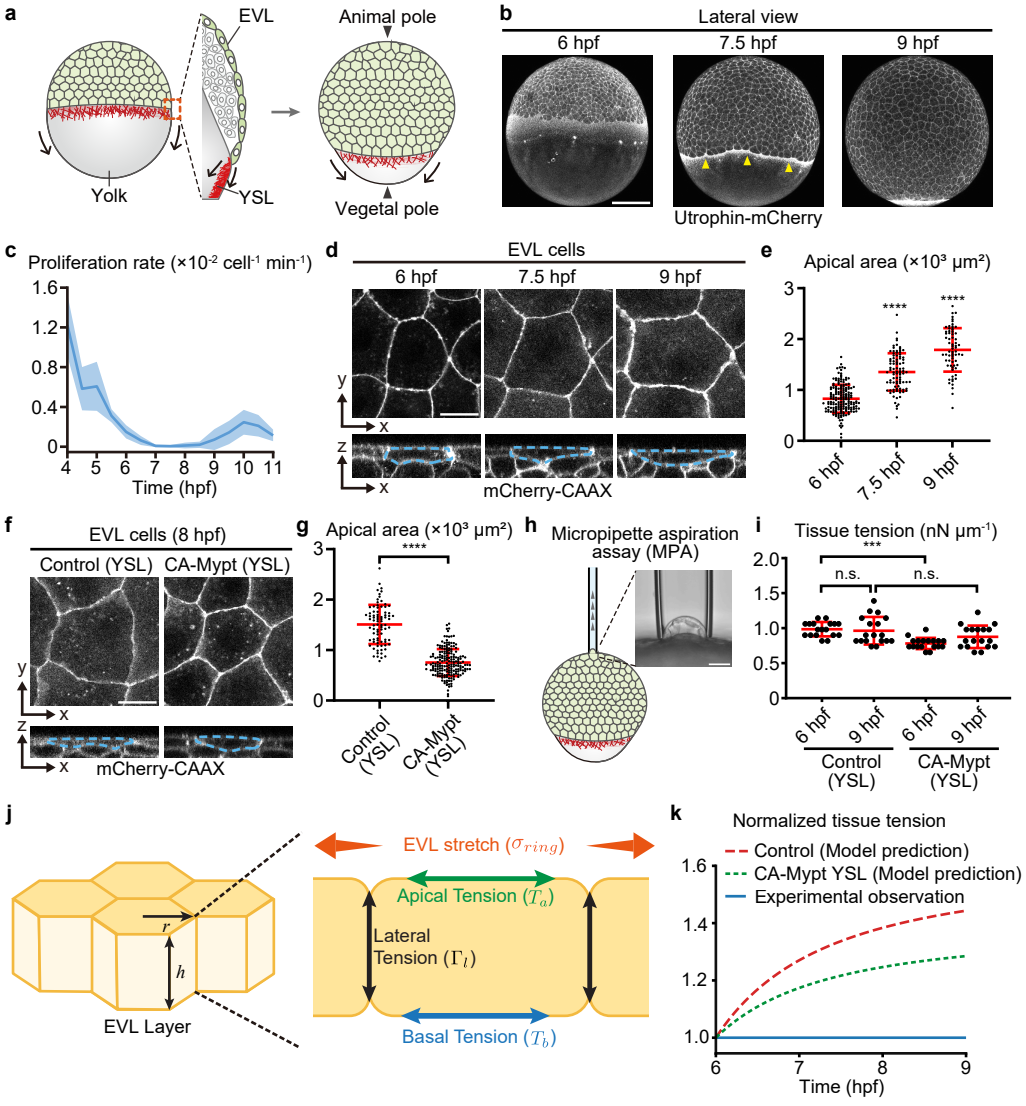
a
EVL
Animal pole
Yolk
YSL
Vegetal pole
b
Lateral view
6 hpf
7.5 hpf
9 hpf
Utrophin-mCherry
c
Proliferation rate (×10-2 cell-1 min-1)
Time (hpf)
d
EVL cells
6 hpf
7.5 hpf
9 hpf
mCherry-CAAX
e
Apical area (×10³ μm²)
6 hpf
7.5 hpf
9 hpf
f
EVL cells (8 hpf)
Control (YSL)
CA-Mypt (YSL)
mCherry-CAAX
g
Apical area (×10³ μm²)
Control (YSL)
CA-Mypt (YSL)
h
Micropipette aspiration assay (MPA)
i
Tissue tension (nN μm-1)
n.s.
6 hpf
9 hpf
Control (YSL)
CA-Mypt (YSL)
j
EVL stretch (σ_{ring})
Apical Tension (T_a)
Lateral Tension (Γ_l)
Basal Tension (T_b)
EVL Layer
k
Normalized tissue tension
Control (Model prediction)
CA-Mypt YSL (Model prediction)
Experimental observation
Time (hpf)

Figure 1. EVL exhibits tissue tension homeostasis during epiboly.

a, A schematic of a zebrafish embryo at 50% (5 hpf, left) and 75% (7.5 hpf, right) epiboly stages. Black arrows mark the direction of EVL epiboly movements. In the left panel, a high magnification cross-section of the region outlined by the orange dashed rectangle is shown. The contraction of the actomyosin ring, positioned within the YSL at the EVL-YSL interface, drives EVL spreading by pulling the EVL margin toward the vegetal pole. EVL, Enveloping layer; YSL, Yolk syncytial layer. **b**, Maximum intensity projection images of a Tg*(actb2: Utrophin-mCherry)* embryo, labeling F-actin, at 6, 7.5, and 9 hours post-fertilization (hpf). Yellow arrowheads indicate the actomyosin ring formed within the YSL. Scale bar, 200 μm. **c**, Line plot of EVL cell proliferation rate normalized by cell number as a function of time during epiboly. Mean ± standard deviation (SD). n = 6 embryos from 3 independent experiments. **d**, Fluorescence images of EVL cells in a Tg*(actb2:mCherry-CAAX)* embryo labeling the plasma membrane at 6, 7.5, and 9 hpf. Top (x-y section) and lateral (x-z section) views are shown for each time point. Representative EVL cells in the lateral views are outlined by blue dashed lines. Scale bar, 20 μm. **e**, Dot plot of EVL cell apical area at 6, 7.5, and 9 hpf. n = 173 cells (6 hpf), n = 91 cells (7.5 hpf), n = 67 cells (9 hpf) from 3 independent experiments. One-way ANOVA followed by Dunnett's multiple comparisons test; ****p < 0.0001 for 6 hpf vs. 7.5 hpf and 6 hpf vs. 9 hpf. **f**, Fluorescence images of EVL cells at 8 hpf in a Tg*(actb2:mCherry-CAAX)* embryo, labeling the plasma membrane, injected with 25 pg H2A-mCherry mRNA (control) or 25 pg H2A-mCherry and 150 pg CA-Mypt mRNA (to reduce actomyosin contraction within the YSL) into the YSL at 3.3 hpf. Top (x-y section) and lateral (x-z section) views are shown for each condition. Representative EVL cells in the lateral views are outlined by blue dashed lines. Scale bar, 20 μm. **g**, Dot plot of EVL cell apical area for the conditions described in **f**. n = 82 cells (control), n = 183 cells (CA-Mypt) from 3 independent experiments. Welch's t-test; ****p < 0.0001. **h**, A schematic of micropipette aspiration assay (MPA) for the measurement of EVL tissue tension. EVL at the animal pole is aspirated by applying negative pressure. The bright-field image on the right shows aspirated EVL. Scale bar, 30 μm. **i**, Dot plot of EVL tissue tension at 6 and 9 hpf, obtained by the MPA on embryos injected with 25 pg H2A-mCherry mRNA (control) or 25 pg H2A-mCherry and 150 pg CA-Mypt mRNA into the YSL (to reduce actomyosin contraction within the YSL) at 3.3 hpf. n = 18 embryos for each condition from 3 independent experiments. One-way ANOVA followed by Tukey's multiple comparisons test; p = 0.9678 for 6 hpf (control) vs. 9 hpf (control); ***p = 0.0003 for 6 hpf (control) vs. 6 hpf (CA-Mypt); p = 0.2674 for 9 hpf (control) vs. 9 hpf (CA-Mypt). **j**, Schematic of the minimal vertex model of EVL cell mechanics. Left: the EVL is represented as a layer of prismatic cells, each described by an apical radius r and height h. Right: tissue tension γ is set by the balance between active apical tension (T_a), basal tension (T_b), and lateral cortical tension (Γ_l), with the actomyosin ring exerting an increasing pulling force σ_{ring} at the EVL margin. From the Young-Laplace relation applied to the prism geometry, $\gamma = 2T_a - \Gamma_l \cdot h/r$. **k**, Tissue tension (normalized to the values at t = 6 hpf) predicted by this geometric model assuming constant apical contractility T_a (i.e., no mechanosensitive regulation). As the ring force drives cell spreading, h/r decreases and γ is therefore expected to rise passively. Dashed lines show the predicted tension in the absence of T_a regulation: for control embryos (red), in which the ring force exceeds tissue tension at t = 6 hpf ($\sigma_{ring}(t = 0) > \gamma_{t=0}$), rapid spreading

is predicted, resulting in a large tension increase. For CA-Mypt YSL embryos (green), in which reduced YSL contractility ($\sigma_{ring}(t = 0) = \gamma_{t=0}$) slows spreading, a smaller but still substantial rise in tension is predicted. Solid blue: experimentally measured tissue tension, which remains approximately constant throughout epiboly. The discrepancy between the predicted and experimentally measured tissue tension profiles motivates an active mechanosensitive circuit that counteracts the passive tension increase.

Figure 2

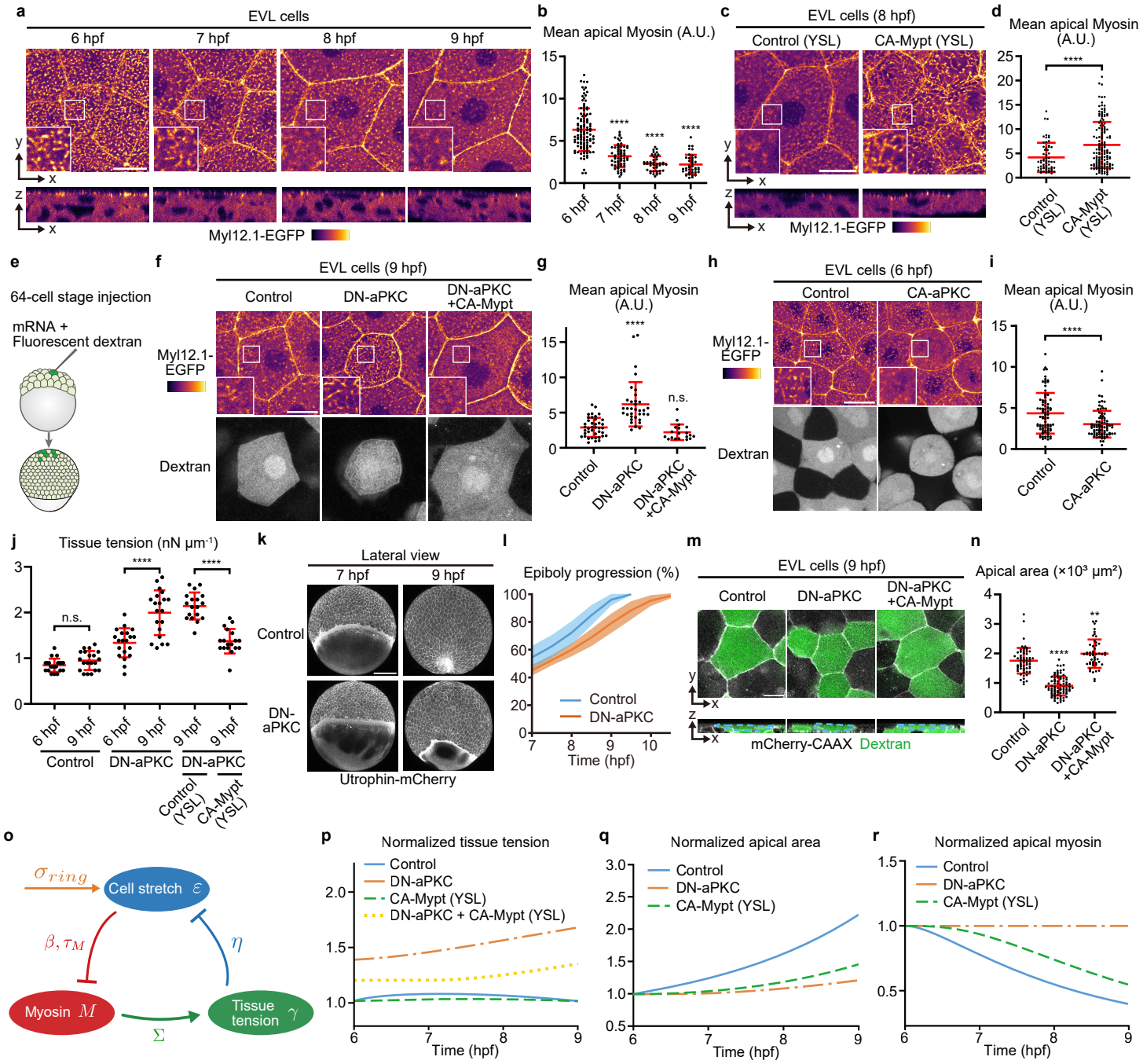
a
EVL cells
6 hpf
7 hpf
8 hpf
9 hpf
Myl12.1-EGFP
b
Mean apical Myosin (A.U.)
c
EVL cells (8 hpf)
Control (YSL)
CA-Mypt (YSL)
d
Mean apical Myosin (A.U.)
e
64-cell stage injection
mRNA +
Fluorescent dextran
f
EVL cells (9 hpf)
Control
DN-aPKC
DN-aPKC +CA-Mypt
Myl12.1-EGFP
Dextran
g
Mean apical Myosin (A.U.)
h
EVL cells (6 hpf)
Control
CA-aPKC
i
Mean apical Myosin (A.U.)
j
Tissue tension (nN μm-1)
n.s.
Control
DN-aPKC
k
Lateral view
7 hpf
9 hpf
Utrophin-mCherry
l
Epiboly progression (%)
Time (hpf)
m
EVL cells (9 hpf)
mCherry-CAAX Dextran
n
Apical area (×10³ μm²)

o
Cell stretch
Myosin M
Tissue tension

p
Normalized tissue tension
Control
DN-aPKC
CA-Mypt (YSL)
DN-aPKC + CA-Mypt (YSL)
Time (hpf)
q
Normalized apical area
r
Normalized apical myosin

Figure 2. Pulling force-dependent reduction in contractility through aPKC activation regulates tissue tension homeostasis.

a, Fluorescence images of EVL cells in a Tg*(actb2:Myl12.1-EGFP)* embryo, labeling Myosin II at 6, 7, 8, and 9 hpf. Top (apical surface projection of x-y section; upper panel) and lateral (x-z section; lower panel) views are shown for each time point. Magnified images of the regions demarcated by white squares are shown in the lower-left corner of each image. Scale bar, 20 μm. **b**, Dot plot of mean apical Myosin II intensity at 6, 7, 8, and 9 hpf. n = 107 cells (6 hpf), n = 60 cells (7 hpf), n = 42 cells (8 hpf), n = 39 cells (9 hpf) from 3 independent experiments. One-way ANOVA followed by Dunnett's multiple comparisons test; ****$p < 0.0001$ for 6 hpf vs. 7, 8, or 9 hpf. **c**, Fluorescence images of EVL cells at 8 hpf in a Tg*(actb2:Myl12.1-EGFP)* embryo injected with 25 pg H2A-mCherry mRNA (control) or 25 pg H2A-mCherry together with 150 pg CA-Mypt mRNA (to reduce actomyosin contraction within the YSL) into the YSL at 3.3 hpf. Top (apical surface projection of x-y section; upper panel) and lateral (x-z section; lower panel) views are shown for each condition. Scale bar, 20 μm. **d**, Dot plot of mean apical Myosin II intensity for the conditions described in **c**. n = 60 cells (control), n = 145 cells (CA-Mypt) from 3 independent experiments. Welch's t-test; ****$p < 0.0001$. **e**, A schematic of 64-cell stage injection: at the 64-cell stage (2 hpf), a single blastomere at the animal pole is injected with mRNA and fluorescent dextran (green). Fluorescently labeled EVL clones are imaged at later stages of epiboly (bottom). **f**, Fluorescence images of EVL cell clones injected at the 64-cell stage with 16.4 pg dextran Alexa Fluor 594 (control), 16.4 pg dextran Alexa Fluor 594 and 19.6 pg DN-aPKC mRNA (DN-aPKC; to reduce aPKC activity), or a combination of 16.4 pg dextran Alexa Fluor 594, 19.6 pg DN-aPKC mRNA, and 9.8 pg CA-Mypt mRNA (DN-aPKC + CA-Mypt, to reduce both aPKC and Myosin II activities) in a Tg*(actb2:Myl12.1-EGFP)* embryo at 9 hpf. Apical surface projection images of Myl12.1-EGFP (top) and dextran Alexa Fluor 594 (bottom) are shown for each condition. Scale bar, 20 μm. **g**, Dot plot of mean apical Myosin II intensity for the conditions described in **f**. n = 40 cells (control), n = 34 cells (DN-aPKC), and n = 19 (DN-aPKC + CA-Mypt) from 3 independent experiments. One-way ANOVA followed by Dunnett's multiple comparisons test; ****$p < 0.0001$ for control vs. DN-aPKC; $p = 0.4282$ for control vs. DN-aPKC + CA-Mypt (not significant, n.s.). **h**, Fluorescence images of EVL cell clones injected at the 64-cell stage with 16.4 pg dextran Alexa Fluor 594 (control) or 16.4 pg dextran Alexa Fluor 594 and 6.5 pg CA-aPKC mRNA (CA-aPKC, to increase aPKC activity) in a Tg*(actb2:Myl12.1-EGFP)* embryo at 6 hpf. Apical surface projection images of Myl12.1-EGFP (top) and dextran Alexa Fluor 594 (bottom) are shown for each condition. **i**, Dot plot of mean apical Myosin II intensity for the conditions described in **h**. n = 83 cells (control), n = 81 cells (CA-aPKC) from 3 independent experiments. Welch's t-test;

****p < 0.0001. **j**, Dot plot of EVL tissue tension measured at the indicated time points, obtained by micropipette aspiration assay in embryos injected with 0.05% Phenol Red (control) or 0.05% Phenol Red and 300 pg DN-aPKC mRNA (DN-aPKC, to decrease aPKC activity) at the 1-cell stage. Embryos injected with 300 pg DN-aPKC mRNA at the 1-cell stage were further injected into the YSL at 3.3hpf with 25 pg H2A-mCherry mRNA (control YSL), or 25 pg H2A-mCherry and 150 pg CA-Mypt mRNA (CA-Mypt YSL). n = 21 embryos for 6 hpf (control), n = 20 embryos for 9 hpf (control), 6 hpf (DN-aPKC), and 9 hpf (DN-aPKC), and n = 18 embryos for DN-aPKC with control and CA-Mypt YSL injections from 3 independent experiments. One-way ANOVA followed by Tukey's multiple comparisons test; p = 0.8888 (n.s.) for 6 hpf (control) vs. 9 hpf (control); ****p < 0.0001 for 6 hpf (DN-aPKC) vs. 9 hpf (DN-aPKC) and for 9 hpf (DN-aPKC; control YSL) vs. 9 hpf (DN-aPKC; CA-Mypt YSL). **k**, Maximum intensity projection images of Tg*(actb2: Utrophin-mCherry)* embryos, labeling F-actin, injected with 0.05% Phenol Red (control, top) or 300 pg DN-aPKC mRNA (DN-aPKC, bottom) at 7 and 9 hpf. Scale bar, 200 μm. **l**, Line plot of EVL epiboly progression as a function of time during epiboly for the conditions described in **k**. Blue and orange lines indicate control and DN-aPKC embryos, respectively. Mean ± SD. n = 9 embryos for each condition from 3 independent experiments. **m**, Fluorescence images of EVL cell clones injected at the 64-cell stage with 16.4 pg dextran fluorescein (control), 16.4 pg dextran fluorescein and 19.6 pg DN-aPKC mRNA (DN-aPKC, to reduce aPKC activity), or 16.4 pg dextran fluorescein together with 19.6 pg DN-aPKC mRNA and 9.8 pg CA-Mypt mRNA (DN-aPKC + CA-Mypt, to reduce both aPKC and Myosin II activities) in a Tg*(actb2:mCherry-CAAX)* embryo at 9 hpf. Top (x-y section; upper panel) and lateral (x-z section; lower panel) views are shown for each condition. Representative EVL cells in the lateral views are outlined by blue dashed lines. Scale bar, 20 μm. **n**, Dot plot of EVL cell apical area for the conditions described in **m**. n = 60 cells (control), n = 82 cells (DN-aPKC), n = 49 cells (DN-aPKC + CA-Mypt) from 3 independent experiments. One-way ANOVA followed by Dunnett's multiple comparisons test; ****p < 0.0001 for control vs. DN-aPKC; **p = 0.0047 for control vs. DN-aPKC + CA-Mypt. **o**, Mechano-chemical circuit of the minimal vertex model (see Supplementary Fig. 3a). Cell stretch (ε) activates aPKC, suppressing Myosin II (M) with sensitivity β and timescale τ_M; Myosin II in turn drives apical contractility (T_a) via a Hill function (coupling constant Σ, exponent n); tissue tension resists further stretch through drag η, closing the negative-feedback loop. YSL ring force σ_{ring} (ramp rate k_f) serves as the external mechanical input. **p**, Line plots of EVL tissue tension (normalized to control at t = 6 hpf) from vertex model simulations for control (full mechanosensing, $\sigma_0 = \gamma_0 + \Delta$; blue, solid), CA-Mypt YSL (reduced ring force during spreading, $\sigma_0 = \gamma_0$, mechanosensing intact; green, dashed), DN-aPKC (no stretch-mediated

Myosin II downregulation, M frozen; orange, dash-dot), and DN-aPKC + CA-Mypt YSL (both perturbations combined, M frozen, $\sigma_0 = \gamma_0$; yellow, dotted) conditions, from 6 to 9 hpf. **q**, Line plots of EVL cell apical area (normalized to control at t = 6 hpf) from vertex model simulations for control, CA-Mypt YSL, and DN-aPKC conditions as in (**p**). **r**, Line plots of apical Myosin II levels (M; assumed to represent apical contractility T_a) from vertex model simulations for control, CA-Mypt YSL, and DN-aPKC conditions as in (**p**). See Methods and parameter table for full details.

Figure 3

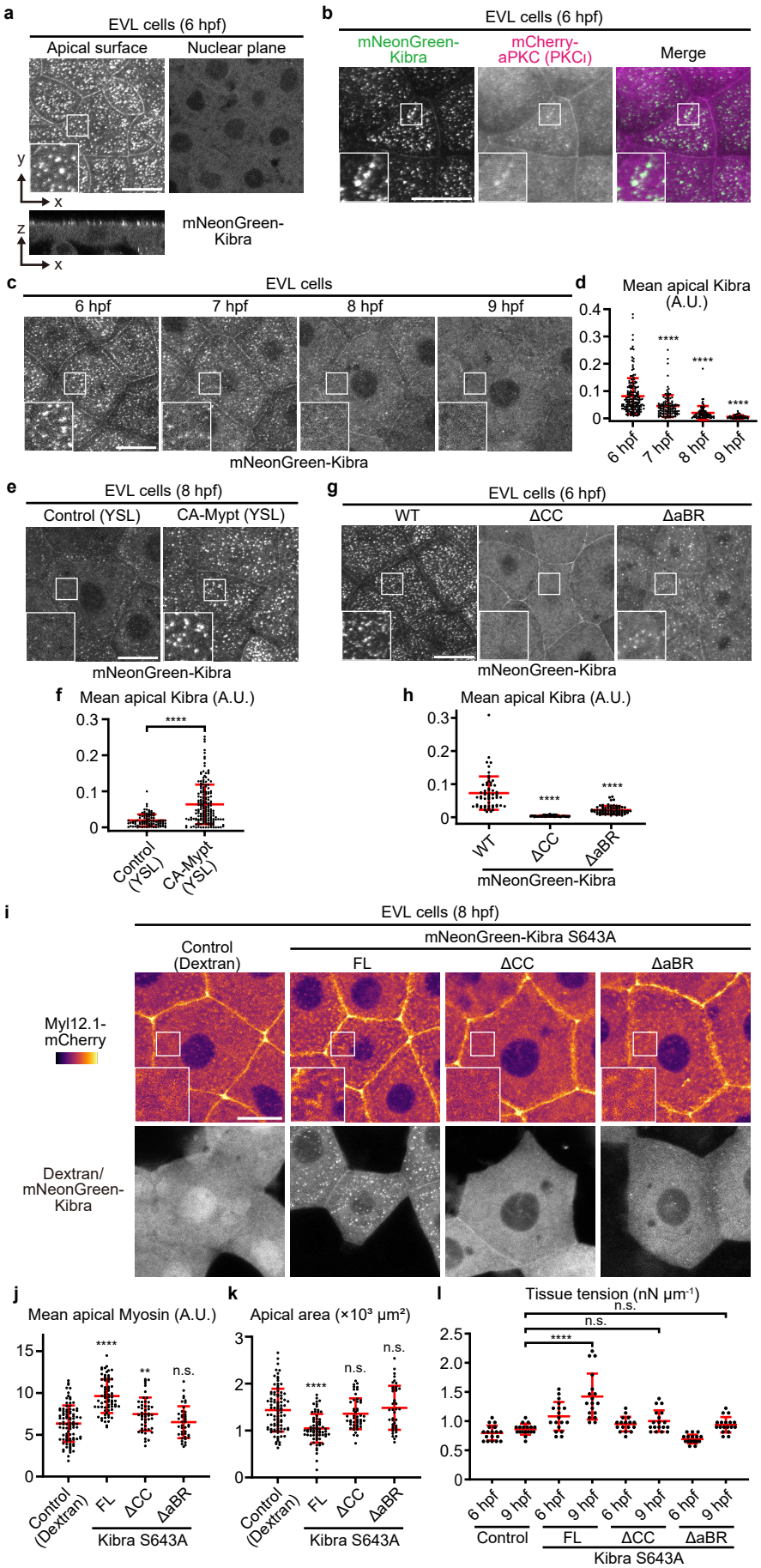
a
EVL cells (6 hpf)
Apical surface
Nuclear plane
y
x
z
x
mNeonGreen-Kibra
b
EVL cells (6 hpf)
mNeonGreen-Kibra
mCherry-aPKC (PKCι)
Merge
c
EVL cells
6 hpf
7 hpf
8 hpf
9 hpf
mNeonGreen-Kibra
d
Mean apical Kibra (A.U.)
0.4
0.3
0.2
0.1
0
****
****
****
6 hpf
7 hpf
8 hpf
9 hpf
e
EVL cells (8 hpf)
Control (YSL)
CA-Mypt (YSL)
mNeonGreen-Kibra
f
Mean apical Kibra (A.U.)
0.3
0.2
0.1
0
****
Control (YSL)
CA-Mypt (YSL)
g
EVL cells (6 hpf)
WT
ΔCC
ΔaBR
mNeonGreen-Kibra
h
Mean apical Kibra (A.U.)
0.3
0.2
0.1
0
****
****
WT
ΔCC
ΔaBR
mNeonGreen-Kibra
i
EVL cells (8 hpf)
Control (Dextran)
mNeonGreen-Kibra S643A
FL
ΔCC
ΔaBR
Myl12.1-mCherry
Dextran/ mNeonGreen-Kibra
j
Mean apical Myosin (A.U.)
15
10
5
0
****
**
n.s.
Control (Dextran)
FL
ΔCC
ΔaBR
Kibra S643A
k
Apical area (×10³ μm²)
3
2
1
0
****
n.s.
n.s.
Control (Dextran)
FL
ΔCC
ΔaBR
Kibra S643A
l
Tissue tension (nN μm⁻¹)
2.5
2.0
1.5
1.0
0.5
0
n.s.
n.s.
****
6 hpf
9 hpf
6 hpf
9 hpf
6 hpf
9 hpf
6 hpf
9 hpf
Control
FL
ΔCC
ΔaBR
Kibra S643A

Figure 3. Pulling force-dependent Kibra condensate dissolution is responsible for the aPKC-mediated reduction in cell contractility and tissue tension homeostasis

a, Fluorescence images of EVL cells in an embryo injected with 200 pg mNeonGreen-wwc1 mRNA at the 1-cell stage to visualize Kibra at 6 hpf. Upper left panel: Apical surface projection of x-y sections (top view). Upper right panel: the x-y section containing nuclei (top view). Lower left panel: lateral view (x-z section); a magnified image of the region demarcated by a white square is shown in the lower-left corner. Scale bar, 20 μm. **b**, Fluorescence images of EVL cells in a Tg*(actb2: mCherry-HA-prkci)* embryo, labeling aPKC, injected with 200 pg mNeonGreen-wwc1 mRNA to visualize Kibra at 6 hpf. Left panel: Kibra. Middle panel: aPKC. Right panel: Merge of Kibra (green) and aPKC (magenta). Scale bar, 20 μm. **c**, Fluorescence images of EVL cells in an embryo injected with 200 pg mNeonGreen-wwc1 mRNA at the 1-cell stage to visualize Kibra at 6, 7, 8, and 9 hpf. Apical surface projection of x-y sections is shown for each time point. Scale bar, 20 μm. **d**, Dot plot of mean apical Kibra intensity at 6, 7, 8, and 9 hpf. n = 182 cells (6 hpf), n = 119 cells (7 hpf), n = 74 cells (8 hpf), n = 49 cells (9 hpf) from 3 independent experiments. One-way ANOVA followed by Dunnett's multiple comparisons test; ****$p < 0.0001$ for 6 hpf vs. 7, 8, or 9 hpf. **e**, Fluorescence images of EVL cells at 8 hpf in an embryo injected with 200 pg mNeonGreen-wwc1 mRNA at the 1-cell stage to visualize Kibra, and injected with 25 pg H2A-mCherry mRNA (control YSL, left panel) or 25 pg H2A-mCherry and 150 pg CA-Mypt mRNA (CA-Mypt YSL; to reduce actomyosin contraction within the YSL, right panel) into the YSL at the 3.3 hpf. Apical surface projection of x-y sections is shown for each condition. Scale bar, 20 μm. **f**, Dot plot of mean apical Kibra intensity for the conditions described in **e**. n = 97 cells (control YSL), n = 176 cells (CA-Mypt YSL) from 3 independent experiments. Welch's t-test; ****$p < 0.0001$. **g**, Fluorescence images of EVL cells in embryos injected at the 64-cell stage with 200 pg (142 amol) mNeonGreen-wwc1, 152 pg (142 amol) mNeonGreen-wwc1 ΔCC mRNA, or 193 pg (142 amol) mNeonGreen-wwc1 ΔaBR mRNA at the 1-cell stage to visualize wild type (WT) Kibra and Kibra deletion mutants at 6 hpf. Apical surface projection of x-y sections is shown for each condition. **h**, Dot plot of mean apical Kibra (WT and deletion mutants) intensities for the conditions described in **g**. n = 59 cells (WT), n = 61 cells (ΔCC), and n = 71 cells (ΔaBR) from at least 3 independent experiments. One-way ANOVA followed by Dunnett's multiple comparisons test; ****$p < 0.0001$ for WT vs. ΔCC or ΔaBR. **i**, Fluorescence images of EVL cell clones injected at the 64-cell stage with 16.4 pg dextran fluorescein (control), 19.6 pg (13.9 amol) mNeonGreen-wwc1 S643A mRNA (FL; full length), 9.9 pg (9.2 amol) mNeonGreen-wwc1 S643A ΔCC mRNA (ΔCC), or 12.7 pg (9.2 amol) mNeonGreen-wwc1 S643A ΔaBR mRNA (ΔaBR) in a Tg*(actb2:myl12.1-mCherry)* embryo, at 8 hpf. Apical surface projection

images of Myl12.1-mCherry (top) and dextran fluorescein or mNeonGreen-Kibra S643A (bottom) are shown for each condition. Scale bar, 20 μm. **j**, Dot plot of mean apical Myosin II intensity for the conditions described in **i**. n = 93 cells (control), n = 71 cells (FL), n = 49 (ΔCC), and n = 41 (ΔaBR) from 3 independent experiments. One-way ANOVA followed by Dunnett's multiple comparisons test; ****p < 0.0001 for control vs. FL; **p = 0.0061 for control vs. ΔCC; p = 0.9619 for control vs. ΔaBR (not significant, n.s.). **k**, Dot plot of EVL cell apical area for the conditions described in **i**. n = 93 cells (control), n = 71 cells (FL), n = 49 (ΔCC), and n = 41 (ΔaBR) from 3 independent experiments. One-way ANOVA followed by Dunnett's multiple comparisons test; ****p < 0.0001 for control vs. FL; p = 0.5849 for control vs. ΔCC (not significant, n.s.); p = 0.8620 for control vs. ΔaBR (n.s.). **l**, Dot plot of EVL tissue tension measured at the indicated time points, obtained by micropipette aspiration assay in embryos injected with 25 pg H2B-GFP mRNA (control), 25 pg H2B-GFP and 200 pg (171 amol) wwc1 S643A mRNA (FL), 25 pg H2B-GFP and 142 pg (171 amol) wwc1 S643A ΔCC mRNA (ΔCC), or 25 pg H2B-GFP and 189 pg (171 amol) wwc1 S643A ΔaBR mRNA (ΔaBR) at the 1-cell stage. n = 18 embryos for each condition, except for ΔCC at 6 hpf (n = 17), from 3 independent experiments. One-way ANOVA followed by Dunnett's multiple comparisons test; ****p < 0.0001 for 9 hpf (control) vs. 9 hpf (FL); p = 0.1774 for 9 hpf (control) vs. 9 hpf (ΔCC), n.s.; p = 0.6288 for 9 hpf (control) vs. 9 hpf (ΔaBR), n.s..

Figure 4

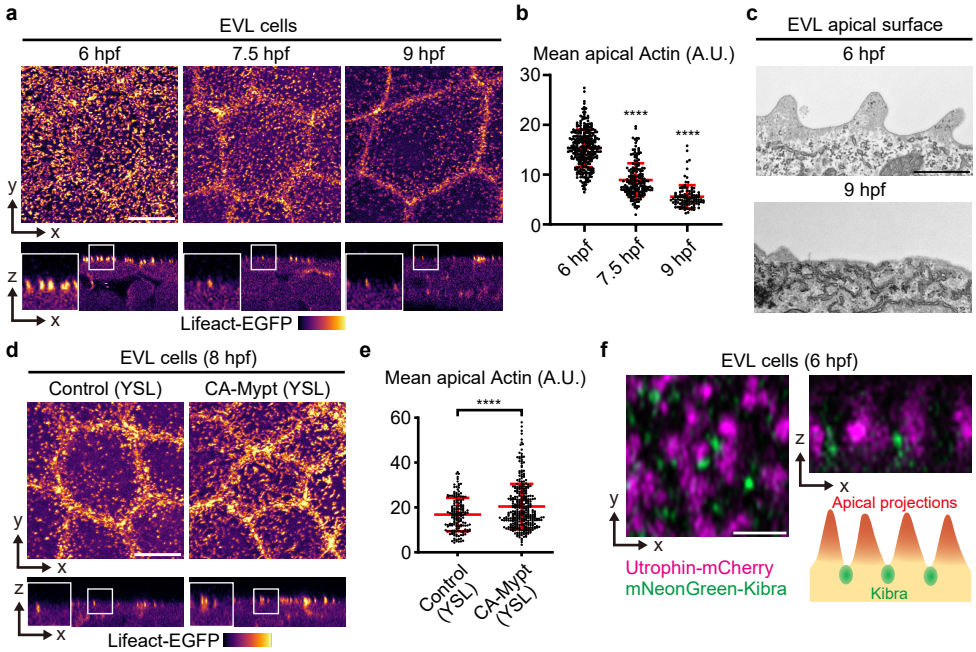
a
EVL cells
6 hpf
7.5 hpf
9 hpf
y
x
z
x
Lifeact-EGFP
b
Mean apical Actin (A.U.)
30
20
10
0
****
****
6 hpf
7.5 hpf
9 hpf
c
EVL apical surface
6 hpf
9 hpf
d
EVL cells (8 hpf)
Control (YSL)
CA-Mypt (YSL)
y
x
z
x
Lifeact-EGFP
e
Mean apical Actin (A.U.)
60
40
20
0
****
Control (YSL)
CA-Mypt (YSL)
f
EVL cells (6 hpf)
y
x
z
x
Utrophin-mCherry
mNeonGreen-Kibra
Apical projections
Kibra

Figure 4. Pulling force triggers disassembly of Kibra-associated apical projections

a, Fluorescence images of EVL cells in a Tg*(actb2:Utrophin-mCherry)* embryo, labeling Actin at 6, 7.5, and 9 hpf. Top (apical surface projection of x-y section; upper row) and lateral (x-z section; lower row) views are shown for each time point. Magnified images of the regions demarcated by white squares are shown in the lower-left corner of each image. Scale bar, 20 μm. **b**, Dot plot of mean apical Actin intensity at 6, 7.5, and 9 hpf. n = 304 cells (6 hpf), n = 180 cells (7.5 hpf), and n = 104 cells (8 hpf) from 3 independent experiments. Dunnett's multiple comparisons test; ****$p < 0.0001$ for 6 hpf vs. 7.5 or 9 hpf. **c**, Electron microscopy images of EVL cells. Apical surfaces of EVL cells at 6 hpf (upper panel) and 9 hpf (lower panel) are shown. Scale bar, 1 μm. **d**, Fluorescence images of EVL cells at 8 hpf in a Tg*(actb2:Utrophin-mCherry)* embryo injected with 25 pg H2A-mCherry mRNA (control YSL) or 25 pg H2A-mCherry plus 150 pg CA-Mypt mRNA (CA-Mypt YSL; to reduce actomyosin contraction within the YSL) into the YSL at 3.3 hpf. Top (apical surface projection of x-y section; upper row) and lateral (x-z section; lower row) views are shown for each condition. Scale bar, 20 μm. **e**, Dot plot of mean apical Actin intensity for the conditions described in **d**. n = 162 cells (control), n = 324 cells (CA-Mypt) from 3 independent experiments. Welch's t-test; ****$p < 0.0001$. **f**, High-resolution fluorescence images of EVL cells at 6 hpf in a Tg*(actb2:Utrophin-mCherry)* embryo injected with 200 pg mNeonGreen-wwc1 mRNA at the 1-cell stage. mNeonGreen-Kibra (green) and Utrophin-mCherry (magenta) are shown in top (x-y section; left panel) and lateral (x-z section; upper right panel) views. A schematic (lower right panel) illustrates Kibra condensates at the base of the apical projections. Scale bar, 2 μm.

Figure 5

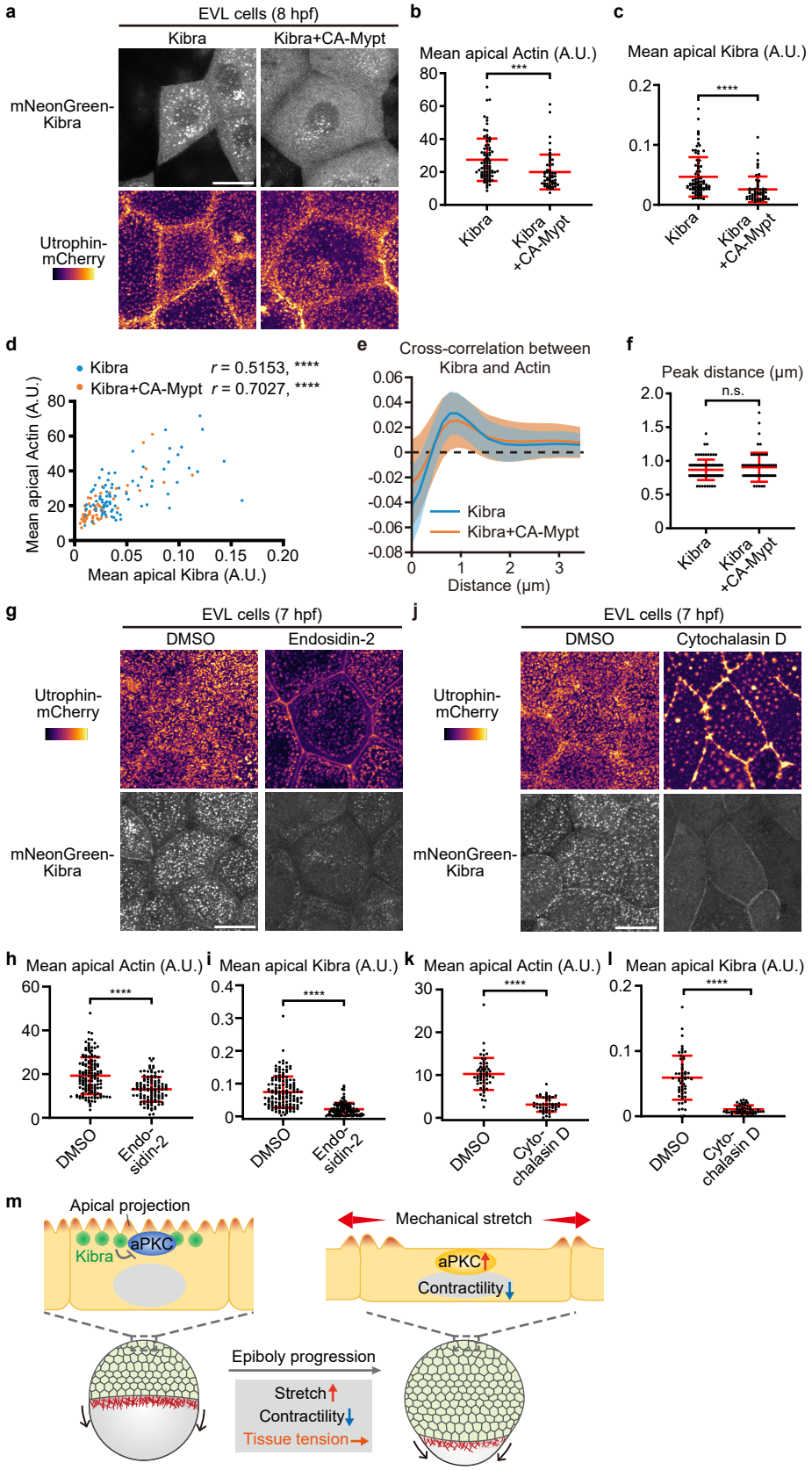
a
EVL cells (8 hpf)
Kibra
Kibra+CA-Mypt
mNeonGreen-Kibra
Utrophin-mCherry
b
Mean apical Actin (A.U.)
***
Kibra
Kibra +CA-Mypt
c
Mean apical Kibra (A.U.)
****
Kibra
Kibra +CA-Mypt
d
Kibra r = 0.5153, ****
Kibra+CA-Mypt r = 0.7027, ****
Mean apical Actin (A.U.)
Mean apical Kibra (A.U.)
e
Cross-correlation between Kibra and Actin
Kibra
Kibra+CA-Mypt
Distance (μm)
f
Peak distance (μm)
n.s.
Kibra
Kibra +CA-Mypt
g
EVL cells (7 hpf)
DMSO
Endosidin-2
Utrophin-mCherry
mNeonGreen-Kibra
j
EVL cells (7 hpf)
DMSO
Cytochalasin D
Utrophin-mCherry
mNeonGreen-Kibra
h
Mean apical Actin (A.U.)
****
DMSO
Endo-sidin-2
i
Mean apical Kibra (A.U.)
****
DMSO
Endo-sidin-2
k
Mean apical Actin (A.U.)
****
DMSO
Cyto-chalasin D
l
Mean apical Kibra (A.U.)
****
DMSO
Cyto-chalasin D
m
Apical projection
Kibra
aPKC
Mechanical stretch
aPKC↑
Contractility↓
Epiboly progression
Stretch↑
Contractility↓
Tissue tension→

Figure 5. Apical projection disassembly triggers Kibra condensate dissolution

a, Fluorescence images of EVL cell clones injected at the 64-cell stage with 13.1 pg mNeonGreen-wwc1 mRNA (Kibra) or 13.1 pg mNeonGreen-wwc1 plus 9.8 pg CA-Mypt mRNA (to reduce actomyosin contraction) in a Tg*(actb2:mCherry-CAAX)* embryo at 8 hpf. Apical surface projection images of x-y sections for mNeonGreen-Kibra (upper row) and Utrophin-mCherry (lower row) are shown for each condition. Scale bar, 20 μm. **b**,**c**, Dot plot of mean apical Actin intensity (**b**) and mean apical Kibra intensity (**c**) for the conditions described in **a**. n = 84 cells (Kibra), n = 57 cells (Kibra + CA-Mypt) from at least 3 independent experiments. Welch's t-test; ***p = 0.0003 for Kibra vs. Kibra + CA-Mypt (mean apical Actin); ****p < 0.0001 for Kibra vs. Kibra + CA-Mypt (mean apical Kibra). **d**, Scatter plot of mean apical Kibra intensity versus mean apical Actin intensity for the conditions described in **a**. Each dot represents a single cell, expressing mNeonGreen-Kibra (blue) or mNeonGreen-Kibra + CA-Mypt (orange). n = 84 cells (Kibra), n = 57 cells (Kibra + CA-Mypt) from at least 3 independent experiments. Spearman's correlation r; ****p < 0.0001 for both Kibra and Kibra + CA-Mypt samples. **e**, Spatial cross-correlations between Kibra and Actin fluorescence images for the conditions described in **a**. Blue (Kibra) and orange (Kibra + CA-Mypt) lines indicate the mean spatial cross-correlation coefficients with SDs. n = 84 cells (Kibra), n = 57 cells (Kibra + CA-Mypt) from at least 3 independent experiments. **f**, Dot plot of the distances corresponding to the local maxima of the correlation coefficients closest to zero spatial shift for the conditions described in **a**. n = 84 cells (Kibra), n = 57 cells (Kibra + CA-Mypt) from at least 3 independent experiments. Welch's t-test; p = 0.2451 (not significant, n.s.). **g**, Fluorescence images of EVL cells at 7 hpf in Tg*(actb2:Utrophin-mCherry)* embryos, labeling Actin, injected with 200 pg mNeonGreen-wwc1 mRNA at the 1-cell stage to visualize Kibra, and subsequently treated with 0.1% DMSO or 100 μM Endosidin-2 at 4 hpf. Apical surface projection images of x-y sections for Utrophin-mCherry (Actin; upper row) and mNeonGreen-Kibra (lower row) are shown for each condition. Scale bar, 20 μm. **h**,**i**, Dot plot of mean apical Actin intensity (**h**) and mean apical Kibra intensity (**i**) for the conditions described in **g**. n = 141 cells (DMSO), n = 112 cells (Endosidin-2) from 3 independent experiments. Welch's t-test; ****p < 0.0001. **j**, Fluorescence images of EVL cells at 7 hpf in Tg*(actb2:Utrophin-mCherry)* embryos, injected with 200 pg mNeonGreen-wwc1 mRNA at the 1-cell stage to visualize Kibra, and subsequently treated with 0.1% DMSO or 10 μg mL^{-1} Cytochalasin D at 5 hpf in Ringer's solution. Apical surface projection images of x-y sections for Utrophin-mCherry (Actin, upper row) and mNeonGreen-Kibra (lower row) are shown for each condition. Scale bar, 20 μm. **k**,**l**, Dot plot of mean apical Actin intensity (**k**) and mean apical Kibra intensity (**l**) for the conditions described in **p**. n = 56 cells (DMSO), n = 49 cells (Cytochalasin

D) from 3 independent experiments. Welch's t-test; ****$p < 0.0001$. **m**, A schematic of tissue tension homeostasis governed by apical domain mechanosensation. At 6 hpf (left), Kibra condensates are formed at the base of actin-based apical projections and inhibits aPKC activity. At 9 hpf (right), mechanical stretching of EVL cells triggered by the YSL pulling forces disassemble apical projections and adjacent Kibra condensates, leading to the activation of aPKC and the decrease of cell contractility. This stretch-induced reduction in cell contractility through apical domain mechanosensation buffers the increase in tissue tension, and thus gives rise to tissue tension homeostasis.